Material Matters™

Vol. 2, No. 4

ALDRICH® Chemistry

Advanced Metals and Alloys

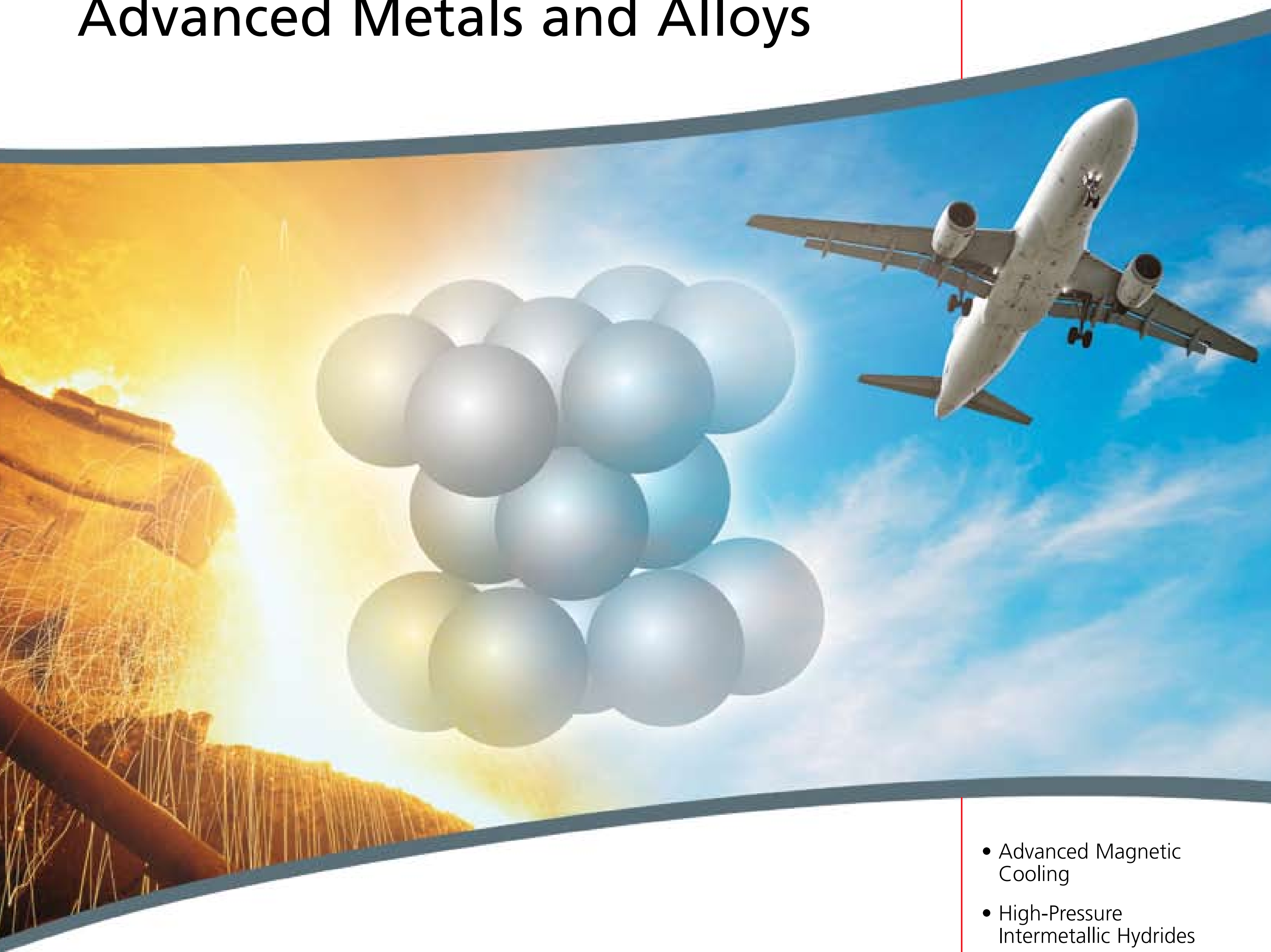

Advancing Technology—
imagine a world without

- Advanced Magnetic Cooling
- High-Pressure Intermetallic Hydrides
- Lightweight Metal Matrix Nanocomposites
- Self-Propagating Reactions By Mechanical Alloying

SIGMA-ALDRICH™

Introduction

No other materials have contributed more to the development of mankind over the millennia than metals and alloys. Throughout centuries, studies of metals belonged to one of the oldest branches of Applied Materials Science–Metallurgy. This changed in the late 19th and early 20th centuries, when applications of metallic materials spread into other areas of science and technology including electronics, energy, aeronautics and space travel, to name a few. Currently, it's impossible to imagine a world in which we could successfully function without metals and alloys.

Traditionally, metals are portrayed as shiny solids, most of which are good conductors of heat and electricity. They are ductile and most will melt at high temperatures. Metal and alloy shapes can easily be changed by mechanical processing, a technique that can be used for the preparation, modification and chemical conversion of metal alloys and composites. Presently, there are 87 known metals, 61 of which are available through Sigma-Aldrich in various forms and modifications; these are highlighted in red in the periodic table chart below. See pages 14–15 for an expanded chart.

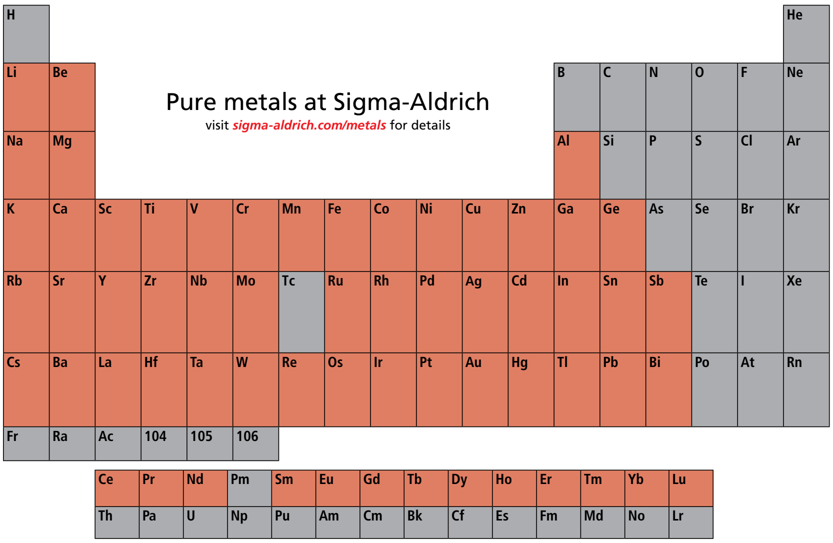

This issue of *Material Matters*™ focuses on metals and alloys for advanced applications including magnetic refrigeration; high-pressure, high-capacity, hydrogen absorbing systems; nanocomposites; and mechanically induced conversion of metallic solids. Leading experts from the Ames Laboratory of the U.S. Department of Energy, Moscow State University, University of Wisconsin–Milwaukee, and University of Maryland discuss recent experimental results and share ideas and techniques associated with metals, alloys, and their applications.

Inside, you'll also find newly introduced products, which include but are not limited to magnetic refrigeration alloys, hydride forming intermetallics, magnetic materials and high-purity rare earth metals and foils. In the "Your Materials Matter" feature, we are pleased to introduce Aligned Multi-Walled Carbon Nanotubes (MWCNTs)—a new Sigma-Aldrich product suggested by Dr. Karl Gross, CEO of Hy-Energy LLC. Our goal at Sigma-Aldrich Materials Science is to provide innovative materials that accelerate your research. For product details and technical information, please visit ***sigma-aldrich.com/matsci***. Have a comment, question or suggestion about *Material Matters*™? Please contact us at **matsci@sial.com**.

Viktor Balema, Ph.D.
Materials Science
Sigma-Aldrich Corporation

About Our Cover

Metals and alloys could be considered the backbone of human civilization. The casting of such metals as copper and tin to make bronze, the first functional metal alloy, paved our way to the modern technological society. Most of the metals crystallize into closely packed cubic (for example, Al, Cu, Fe) or hexagonal crystal lattices (shown on the cover, for example, Gd, Ti, Zr, rare earth metals), which are largely responsible for their remarkable properties. The cover shows metal casting, the beginning of a long technological process that concludes in such marvels as airplanes.

Material Matters™
Vol. 2 No. 4

Aldrich Chemical Co., Inc.
Sigma-Aldrich Corporation
6000 N. Teutonia Ave.
Milwaukee, WI 53209, USA

To Place Orders

Telephone	800-325-3010 (USA)
FAX	800-325-5052 (USA)

Customer & Technical Services

Customer Inquiries	800-325-3010
Technical Service	800-231-8327
SAFC™	800-244-1173
Custom Synthesis	800-244-1173
Flavors & Fragrances	800-227-4563
International	414-438-3850
24-Hour Emergency	414-438-3850
Web Site	sigma-aldrich.com
Email	aldrich@sial.com

Subscriptions

To request your **FREE** subscription to *Material Matters*, please contact us by:

Phone: **800-325-3010** (USA)

Mail: **Attn: Marketing Communications**
Aldrich Chemical Co., Inc.
Sigma-Aldrich Corporation
P.O. Box 355
Milwaukee, WI 53201-9358

Email: **sams-usa@sial.com**

International customers, please contact your local Sigma-Aldrich office. For worldwide contact information, please see back cover.

Material Matters is also available in PDF format on the Internet at **sigma-aldrich.com/matsci**.

"Your Materials Matter."

Joe Porwoll, President
Aldrich Chemical Co., Inc.

Do you have a compound that you wish Sigma-Aldrich could list to help materials research? If it is needed to accelerate your research, it matters—please send your suggestion to matsci@sial.com and we will be happy to give it careful consideration.

Aligned Multi-Walled Carbon Nanotubes (MWCNTs)

Dr. Karl Gross, of Hy-Energy LLC, kindly suggested that high-quality carbon nanotube arrays are needed for research and development of high-sensitivity gas sensors. We are pleased to offer highly aligned arrays of multi-wall carbon nanotubes (MWCNTs) as new products in our catalog. These arrays, available on silicone (Aldrich Product No. **687804**) or copper (Aldrich Product No. **687812**) substrates, can provide a unique platform for a wide range of materials research and development, including gas adsorption sensor and sensor substrates,[1] catalysts, electron emission sources,[2] and battery and capacitor development.[3]

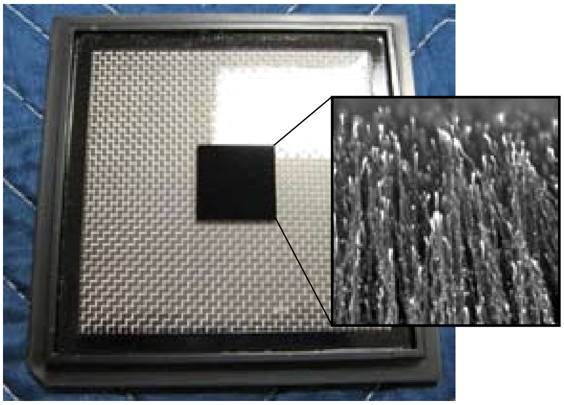

CNT array (black square) in the semiconductor grade package. Inset shows SEM image of the vertically aligned MWCNTs.

Carbon nanotube array, multi-walled, vertically aligned, on silicon wafer substrate

687804-1EA

Carbon nanotube array, multi-walled, vertically aligned, on copper substrate

687812-1EA

Features:

- 99.9% as MWCNT
- CNT diameters are 100 nm ± 10 nm
- CNT lengths are 30 μm ± 3 μm
- Array density ~2 x 10^9 MWCNT/cm^2
- Array dimensions 1 sq. cm
- Grown by plasma-enhanced CVD (PECVD)
- Grown with the nickel catalyst tip intact
- Packaged in a clean room; stored, and shipped in semiconductor grade packaging.

References:

(1) Collins, P.G., Bradley, K. Ishigami, M. Zettl, A., *Science*, **2000**, 287, 1801. (2) Bonard, J. M., Stockli, T., Maier, F., De Herr, W. A., Chatelain, A., Ugarte, D., Salvetat, J. P., Forro, L., *Physical Review Letters*, **1998**, 81, 1441. (3) Frackowiak, E., Gautier, S., Gaucher, H., Bonnamy, S., Beguin, F., *Carbon*, **1999**, 37, 61

Advanced Metals and Alloys Featured in This Issue

Advanced Materials for Magnetic Cooling

Prof. V. K. Pecharsky and Prof. K. A. Gschneidner, Jr.

Ames Laboratory, Iowa State University

Introduction

Today, near-room-temperature refrigeration is almost entirely based on a vapor-compression refrigeration cycle. Over the years, all parts of a commercial refrigerator, such as the compressor, heat exchangers, refrigerant, and packaging, have been improved considerably due to the extensive research and development efforts carried out by academia and industry. However, the achieved and anticipated improvements in conventional refrigeration technology are incremental since this technology is already near its fundamental limit of energy efficiency. Furthermore, chlorofluorocarbons, hydrofluorocarbons, and other chemicals used as refrigerants eventually escape into the environment promoting ozone layer depletion and global warming. In general, liquid chemical-based refrigeration is a major factor contributing to deleterious, cumulative changes in the global climate.

Refrigeration is based on the use of a working body that changes its temperature in response to certain thermodynamic triggers to cool an object. These variations must be achieved quickly, repeatedly, reversibly, and with *minimum energy losses*. Since a magnetic field effectively couples to magnetic moments of individual atoms in a solid, magnetic field is one of the common thermodynamic variables that can alter the temperature of a magnetic solid. Heating and cooling of soft ferromagnetic materials in response to increasing and decreasing magnetic fields, respectively, has been known since the latter part of the 19th century when Warburg reported small but measurable reversible temperature changes in pure iron in response to magnetic field changes.[1] Today, this phenomenon is recognized as the *Magnetocaloric Effect* (MCE) and materials exhibiting large, reversible temperature changes in response to changing magnetic fields are usually referred to as *magnetocaloric materials*. The efficiency gain when replacing a mechanical process (compression and expansion of a vapor) with an electronic process (magnetization and demagnetization of a solid) to obtain a reversible change of temperature is substantial, thus making *magnetic refrigeration* one of the few viable, energy-efficient solid-state cooling technologies.

Magnetocaloric Effect

The magnetocaloric effect occurs when a magnetic sublattice is coupled with an external magnetic field, affecting the magnetic part of the total entropy of a solid. Similar to the isothermal compression of a gas, during which the positional disorder and the corresponding component of the total entropy of the gaseous system are suppressed, exposing a paramagnet near absolute zero temperature or a ferromagnet near its Curie temperature, T_C, to a change in magnetic field (B) from zero to any non-zero value, or in general, from any initial value B_i to a final higher value B_f ($\Delta B = B_f - B_i > 0$) greatly reduces disorder of a spin system. Thus, the magnetic part (S_M) of the total entropy (S) is substantially lowered. In a reversible process, which resembles the expansion of the gas at constant temperature, isothermal demagnetization ($\Delta B < 0$) restores the zero field magnetic entropy of a system. The magnetocaloric effect, therefore, can be quantified as an extensive thermodynamic quantity, which is the isothermal magnetic entropy change, ΔS_M.

When a gas is compressed adiabatically, its total entropy remains constant whereas, velocities of the constituent molecules, and therefore, the temperature of the gas both increase. Likewise, the sum of the lattice and electronic entropies of a solid must change by $-\Delta S_M$ as a result of adiabatic magnetization (or demagnetization) of the material, thus leading to an increase (decrease) of the vibrational entropy of the lattice. This brings about an adiabatic temperature change, ΔT_{ad}, which is an intensive thermodynamic quantity that is also used to measure and quantify the magnetocaloric effect.

The Standard Magnetocaloric Material—Gd

For near-room-temperature applications, the rare earth metal Gd is the benchmark magnetic refrigerant material. It exhibits excellent magnetocaloric properties that are difficult to improve upon. Not surprisingly, the metal has been employed in early demonstrations of near-ambient cooling by the magnetocaloric effect.[2–4] Gadolinium (Aldrich Prod. Nos. **263087**, **261114**, **263060**, **691771**) was used as the refrigerant powering the first successful proof-of-principle refrigerator device.[4] Metallic gadolinium has constituted the whole or at least a major part of every magnetic regenerator bed in nearly every near-room-temperature magnetic cooling machine built and tested to date.[5,6]

The isothermal magnetic entropy change in Gd, calculated from heat capacity and magnetization data, is shown in **Figure 1**.[7] The MCE computed from the two different types of experimental data match well (as shown by the results for the 2T and 5T magnetic field changes), provided experimental measurements have been performed with sufficient accuracy. Furthermore, Figure 1 shows that as the magnetic field increases, the derivative of the MCE with respect to the magnetic field decreases (both ΔT_{ad} and ΔS_M are nearly proportional to $B^{2/3}$, i.e. $d(\mathrm{MCE})/dB \propto B^{-1/3}$). In other words, the highest specific magnetocaloric effect (i.e. the MCE per unit field change) always occurs near zero magnetic field. The intensive MCE of Gd is illustrated for four different magnetic field changes in **Figure 2**.[7] Similar to ΔS_M, ΔT_{ad}, peaks at T_C and $d(\Delta T_{ad})/dB$ is also substantially reduced as B increases. The nearly $B^{2/3}$ dependence of the ΔT_{ad} of Gd is illustrated in **Figure 3**, where experimental measurements reported by numerous authors exhibit an excellent fit of the MCE data to the $B^{0.7}$ behavior.

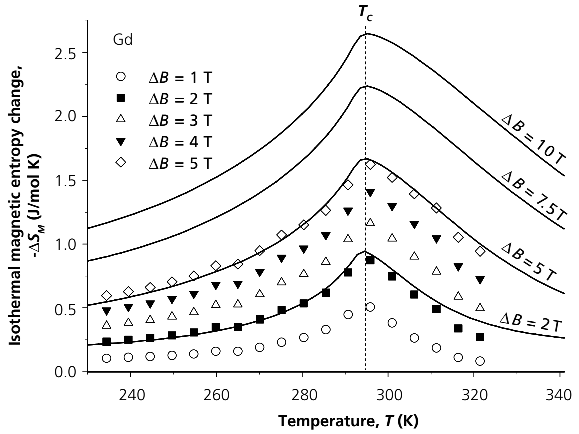

Figure 1. A comparison of the magnetocaloric effect (isothermal magnetic entropy change, ΔS_M) for Gd calculated from magnetization (symbols) and heat capacity data (solid lines).

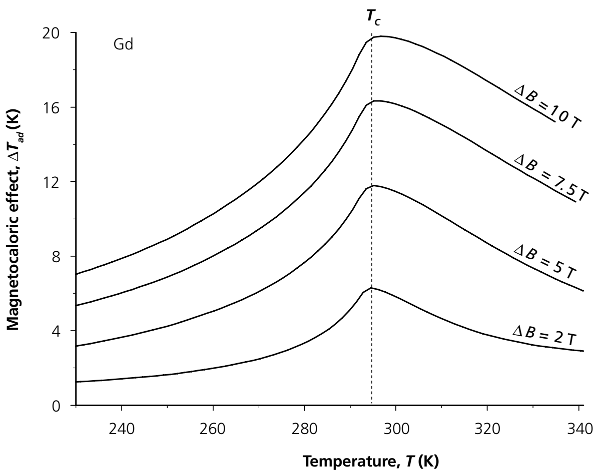

Figure 2. The magnetocaloric effect (adiabatic temperature change, ΔT_{ad}) for Gd calculated from heat capacity data.

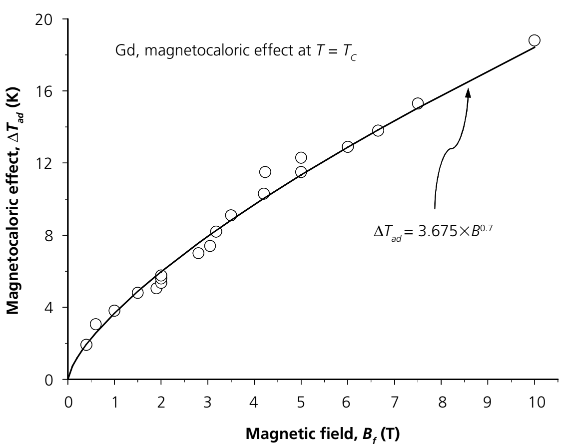

Figure 3. The magnetocaloric effect for Gd at its Curie temperature, shown as a function of the final magnetic field, B_f, for $B_i = 0$. The symbols represent values either measured directly or calculated from heat capacity data by different authors.[7] The line is the least squares fit assuming power-law dependence of the MCE on the magnetic field.

The behavior of the magnetocaloric effect of Gd illustrated in Figures 1–3 is quite universal for materials with second-order paramagnetic-ferromagnetic phase transformations. The differences between the MCE in Gd and in those of other second-order phase transition materials mainly lie in differences in the absolute values of the magnetocaloric effect for the same magnetic field change, the temperature of the peak, and how quickly the derivative, d(MCE)/dB, is suppressed by the increasing magnetic field. To illustrate this universality, **Figure 4** shows the adiabatic temperature change of a few different magnetocaloric materials, all of which order magnetically via second-order transformations at various temperatures ranging from ~14 K to ~294 K. One of the five materials—elemental dysprosium—orders antiferromagnetically but magnetic fields exceeding ~2T transform the metal into a collinear ferromagnet, thus the behavior of the MCE near the Neél temperature of Dy (Aldrich Prod. Nos. **261076**, **263028**, **263036**) is nearly identical to that of other ferromagnets.

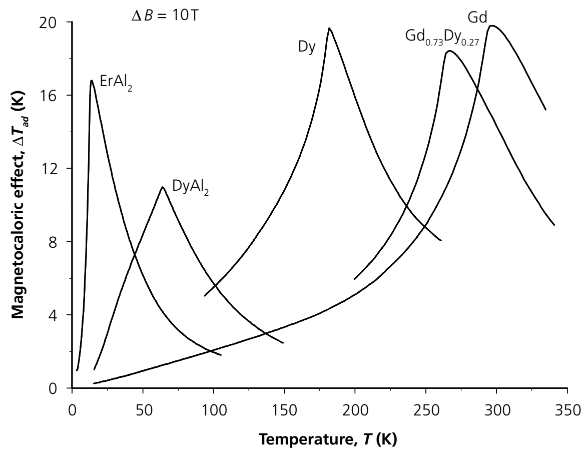

Figure 4. The magnetocaloric effect in $ErAl_2$,[8] $DyAl_2$,[8] Dy,[9] $Gd_{0.73}Dy_{0.27}$,[10] and Gd[7] calculated from heat capacities measured in a zero and 10T magnetic field.

Giant Magnetocaloric Effect

Rising interest in both the fundamental science and potential applications of advanced magnetocaloric materials has been sparked by recent discoveries of new compounds exhibiting a magnetocaloric effect much larger (in some cases by a factor of two to three) than those found in previously known compounds, including elemental Gd. The most notable examples that constitute a pool of advanced magnetocaloric materials are FeRh,[11] $La_{0.8}Ca_{0.2}MnO_3$,[12] and $Gd_5Si_2Ge_2$ and the related $Gd_5(Si_xGe_{4-x})$ alloys;[13,14] the latter references also coined the phrase "the giant magnetocaloric effect" (GMCE) materials. A few years later, several other families of materials have been shown to also exhibit the giant magnetocaloric effect at temperatures close to ambient. These include $Tb_5Si_2Ge_2$,[15] MnAs and $MnAs_{1-x}Sb_x$ compounds,[16] $La(Fe_{1-x}Si_x)_{13}$ alloys and their hydrides $La(Fe_{1-x}Si_x)_{13}H_y$,[17] $MnFeP_{0.45}As_{0.55}$ and related $MnFeP_xAs_{1-x}$ alloys,[18] and $Ni_{2\pm x}Mn_{1\pm x}Ga$ ferromagnetic shape memory alloys.[19]

Today, it has been well established that the giant magnetocaloric effect arises from magnetic field induced magnetostructural first-order transformations. Upon the application of a magnetic field, the magnetic state of a compound changes from a paramagnet or an antiferromagnet to a nearly collinear ferromagnet simultaneously with either a martensitic-like structural distortion, or is accompanied by a phase volume discontinuity but without a clear crystallographic modification. When the system undergoes a first-order phase transition, the behavior of the total entropy as a function of temperature reflects a discontinuous (in reality, almost always continuous, except for some ultra-pure lanthanides) change of entropy at a critical temperature, T_c.

The behavior of both the extensive and intensive measures of the giant magnetocaloric effect in first-order phase transition materials is different when compared to the conventional magnetocaloric effect in second-order phase transition compounds, as can be easily seen in **Figure 5** when compared to Figures 1 and 2. First, especially for small magnetic fields, the giant magnetocaloric effect is much larger than the conventional MCE (see a recent review by Gschneidner et al.[20]). Second, the width of the GMCE becomes broader as ΔB increases, but it broadens asymmetrically on the high temperature side of the magnetic ordering phase transition. Third, as ΔB increases, both the ΔS_M and ΔT_{ad} increase rapidly for small fields with the corresponding derivatives ($\partial\Delta S_m/\partial\Delta B$ and $\partial\Delta T_{ad}/\partial\Delta B$) exhibiting a clear tendency towards saturation. As a matter of fact, when the magnetic field is strong enough to complete the transformation, the magnitudes of the ΔS_M discontinuities remain identical. These discontinuities correspond to the entropies of phase transformations (that include both the magnetic and structural contributions, Figure 5), and the observed modest rise of the background under ΔS_M peaks is due to magnetic field effects on the magnetic entropy of the material in the ferromagnetic state, just as in other materials exhibiting conventional MCE. As was shown recently,[9] the calculated magnetic entropy change in Dy in the vicinity of its first-order magnetic phase transition at T = 90 K matches the entropy change of the spontaneous FM → AFM phase transformation measured directly in a zero magnetic field to within 2%.

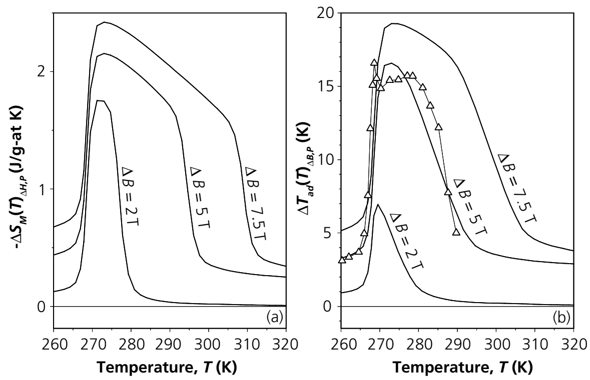

Figure 5. The giant magnetocaloric effects in $Gd_5Si_2Ge_2$ as represented by (a) extensive (ΔS_M) and (b) intensive (ΔT_{ad}) measures, shown as functions of temperature for three different magnetic field changes: from 0 to 2T, from 0 to 5T, and from 0 to 7.5T calculated from heat capacity data. The open triangles in (b) represent the GMCE measured directly for a magnetic field change from 0 to 5T.

Obviously, the conventional (Figures 1 and 2) and giant (Figure 5) MCE's are considerably different, and the difference between them should be primarily ascribed to the absence and the presence of a structural change in second-order and first-order materials, respectively. The giant MCE is achieved due to the concomitant change of the entropy during the structural transformation, ΔS_{str}. As a result, the observed giant magnetocaloric effect ΔS_M is the sum of the conventional magnetic entropy-driven process (ΔS_m) and the difference in the entropies of the two crystallographic modifications (ΔS_{str}) of a solid. In other words, it is the second term of the right hand side of the following equation that is at the core of the giant magnetocaloric effect.

$$\Delta S_M = \Delta S_m + \Delta S_{str}$$

Advanced Magnetocaloric Materials and Other Possible Applications

The discovery of the giant magnetocaloric effect and extensive characterization of multiple families of GMCE materials are indeed extremely important developments both in the science of the magnetocaloric effect and, potentially, in its application to near-room-temperature cooling. The overlapping contribution from the crystallographic and related electronic changes in the lattice may account for 50% or more of the total MCE (as quantified by the isothermal magnetic entropy change) in magnetic fields of 5T and below. More significantly, the relative contribution from the structural entropy change ΔS_{str} to ΔS_M increases as the magnetic field decreases so long as the final magnetic field (B_f) is strong enough to complete the magnetostructural transition. We refer the interested reader to the latest review[20] for a chart schematically comparing the magnetocaloric effects in first-order phase transition compounds (GMCE materials) and second-order phase transition compounds (MCE materials) and for a list of references (including earlier reviews) where one can find a comprehensive summary describing today's state-of-the-art magnetocaloric materials.

Bonding, structural, electronic, and magnetic changes, which occur in the giant magnetocaloric effect systems, bring about some extreme changes of the materials' behavior resulting in a rich variety of unusually powerful magneto-responsive properties in addition to the GMCE. In particular, these include the colossal magnetostriction (which can be as much as ten times larger than that in Terfenol-D), and the giant magnetoresistance (which is comparable to that found in artificial multi-layered thin films). We note here that the giant magnetoresistance observed near the corresponding phase transformation temperatures may be either positive or negative depending upon the nature of the giant magnetocaloric effect material. An easy manipulation of the chemical composition, for example the Si to Ge ratio in $Gd_5(Si_xGe_{4-x})$ alloys, enables one to precisely tune these materials to display the largest required response almost at any temperature between ~4 and ~300 K. Similar effects may be found when the hydrogen concentration in $La(Fe_{1-x}Si_x)_{13}H_y$ alloys, or the As to Sb ratio in $MnAs_{1-x}Sb_x$ compounds is changed.

Advanced magnetocaloric materials, no doubt, should exist in other solid systems where structural changes are coupled with ferromagnetic ordering, and therefore, can be triggered by a magnetic field. Materials designed to maximize the entropy difference between the low-magnetic-field and high-magnetic-field phases, i.e. those that exhibit large entropy of a structural transformation, ΔS_{str}, in addition to a large magnetic entropy change ΔS_m, are expected to exhibit the strongest MCE's in the weakest magnetic fields. Furthermore, it is important that these materials also have large ΔT_{ad}, which can be achieved by maximizing the effect of a magnetic field on the phase transition temperature. Despite numerous studies of first-order phase transition materials, much remains to be learned about the fundamentals of the giant magnetocaloric effect. The most critical issues are how to control both the magnetic and lattice contributions to the phenomenon in order to maximize the magnetocaloric effect in reasonably small magnetic fields (on the order of 1 to 2 Tesla), and how to reduce some potentially deleterious effects such as time dependence and irreversibility associated with the GMCE, thus paving the way to the applicability of these advanced magnetic materials in emerging magnetic refrigeration technology.

Acknowledgments

Work at the Ames Laboratory is supported by the Office of Basic Energy Sciences, Materials Sciences Division of the U. S. Department of Energy under Contract No. DE-AC02-07CH11358 with Iowa State University of Science and Technology.

References:

(1) Warburg, E., *Ann. Phys. (Leipzig)* **1881**, *13*, 141. (2) Brown, G. V., *J. Appl. Phys.* **1976**, *46*, 3673. (3) Green, G.; Chafe, J.; Stevens J.; Humphrey, J. *Adv. Cryo. Engin.* **1990**, *35*, 1165. (4) Zimm, C.; Jastrab A.; Sternberg A.; Pecharsky V.; Gschneidner K. Jr.; Osborne M.; Anderson I. *Adv. Cryo. Engin.* **1998**, *43*, 1759. (5) Gschneidner, K. A., Jr.; Pecharsky, V. K.; In: Proc. 2nd Intern. Conf. Magn. Refr. Room Temp, Portoroz, Slovenia, April 11-13, 2007, A. Poredoš, A. Šarlah, Eds. (Int. Inst. Refr. IIR/IIF, Paris, France, 2007) p. 9. (6) Tishin, A. M.; Spichkin, Y. I. *The Magnetocaloric Effect and its Applications* (Institute of Physics Publishing: Bristol, 2003). (7) Dank'ov, S. Yu.; Tishin, A. M.; Pecharsky, V. K.; Gschneidner, K. A., Jr. *Phys. Rev. B* **1998**, *57*, 3478. (8) Gschneidner, K. A., Jr.; Pecharsky, V. K.; Malik, S. K. *Adv. Cryo. Engin.* **1996**, *42A*, 465. (9) Chernyshov, A. S.; Tsokol, A. O.; Tishin, A. M.; Gschneidner, K. A., Jr.; Pecharsky, V. K. *Phys. Rev. B* **2005**, *71*, 184410. (10) Pecharsky, V. K.; Gschneidner, K. A., Jr. unpublished. (11) Annaorazov, M. P.; Asatryan, K. A.; Myalikgulyev, G.; Nikitin, S. A.; Tishin, A. M.; Tyurin, A. L. *Cryogenics* **1992**, *32*, 867. (12) Guo, Z. B.; Du, Y. W.; Zhu, J. S.; Huang, H.; Ding, W. P.; Feng, D. *Phys. Rev. Lett.* **1997**, *78*, 1142. (13) Pecharsky, V. K.; Gschneidner, K. A., Jr. *Phys. Rev. Lett.* **1997**, *78*, 4494. (14) Pecharsky, V. K.; Gschneidner, K. A., Jr. *Appl. Phys. Lett.* **1997**, *70*, 3299. (15) Morellon, L.; Magen, C.; Algarabel, P. A.; Ibarra, M. R.; Ritter, C. *Appl. Phys. Lett.* **2001**, *79*, 1318. (16) Wada, H.; Tanabe, Y. *Appl. Phys. Lett.* **2001**, *79*, 3302. (17) Fujita, A.; Fujieda, S.; Hasegawa, Y.; Fukamichi, K. *Phys. Rev. B* **2003**, *67*, 104416. (18) Tegus, O.; Brück, E.; Buschow, K. H. J.; de Boer, F. R. *Nature (London)* **2002**, *415*, 150. (19) Albertini, F.; Canepa, F.; Cirafici, S.; Franceschi, E. A.; Napoletano, M.; Paoluzi, A.; Pareti, L.; Solzi, M. *J. Magn. Magn. Mater.* **2004**, *272–276*, 2111. (20) Gschneidner, K. A., Jr.; Pecharsky, V. K.; Tsokol, A. O. *Rep. Progr. Phys.* **2005**, *68*, 1479.

Materials for Magnetic Cooling

Name	Chem. Composition, Physical Form	Curie Temperature	Prod. No.
Gadolinium-Silicon-Germanium Alloy, $Gd_5Si_2Ge_2$	$Gd_5Si_2Ge_2$, pieces/coarse powder	~ 270 K	**693510-1G**
Gadolinium-Silicon-Germanium Alloy, $Gd_5Si_{0.5}Ge_{3.5}$	$Gd_5Si_{0.5}Ge_{3.5}$, pieces/coarse powder	~ 70 K	**693502-1G**
Dysprosium-Erbium-Aluminum Alloy, $Dy_{0.8}Er_{0.2}Al_2$	$Dy_{0.8}Er_{0.2}Al_2$, pieces/coarse powder	below 60 K	**693499-1G**
Gadolinium	Gd, 99.99% (REM)*	293 K	**691771-10G**

*Rare earth metals

Ultra High-Purity Metals for the Preparation of Magnetic Refrigeration Materials

Metal	Physical Form	Comments	Purity, %	Prod. No
Antimony (Sb)	Beads	1–2 mm	99.999	**266604-25G** **266604-100G**
Calcium (Ca)	Dendritic pieces	purified by distillation	99.99	**441872-5G** **441872-25G**
Gallium (Ga)	Low melting metal	m.p. 30 °C	99.999	**263273-1G** **263273-10G** **263273-50G**
			99.9995	**203319-1G** **203319-5G** **203319-25G**
Germanium (Ge)	Powder	–100 mesh	99.999	**327395-5G** **327395-25G**
	Chips		99.9998	**263230-10G** **263230-50G**
Manganese (Mn)	Powder	~10 µm	99.99	**463728-25G** **463728-100G**
Rhodium (Rh)	Powder	particle size not specified	99.99	**204218-250MG** **204218-1G**
Silicon (Si)	Powder	–60 mesh	99.999	**267414-5G** **267414-25G**
		particle size not specified	99.9995	**475238-5G** **475238-25G**

For more information about these and other related materials, please visit ***sigma-aldrich.com/metals***.

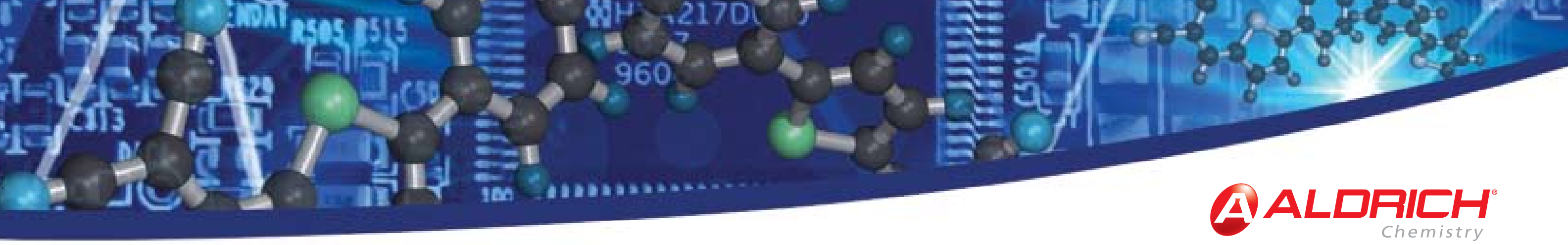

ALDRICH Chemistry

Magnetic Alloys and Intermetallics

Magnetic alloys and intermetallics are metallic materials capable of producing a constant magnetic field for a prolonged period of time. There are only a limited number of chemical elements that can produce alloys with permanent magnetic properties at ambient temperature; Fe, Ni, Co and rare earth metals are the most important ones.

The magnetic materials offered by Sigma-Aldrich are capable of producing a high magnetic field with a low mass. They are also fairly stable against influences to demagnetize them. Major properties of our materials are described by the parameters shown below.

Maximum Energy Product, $B(H)_{max}$: The point on the demagnetization curve where the product of Magnetic Induction (B) and Magnetic Field Strength (H), reaches a maximum and the volume of magnetic material required to project a given energy is minimum.

Residual Induction, B_r: The point at which the hysteresis loop crosses the B axis at zero magnetizing force and represents the maximum magnetic flux output from the given material.

Coercive Force, H_c: The demagnetizing force necessary to reduce observed induction, B, to zero after the magnet has previously been brought to saturation.

Maximum Operation Temperature: Maximum temperature at which magnetic materials still retain their magnetic properties.

Magnetic Alloys

Type	Name	Comments	Prod. No.
Samarium-Cobalt Alloys	$SmCo_5$, alloy 18, Discs 10X6 mm	$B(H)_{max}$ =140 kJ/m^3 (18 MGsOe), B_r = 0.87T (8.7kGs), H_{cb} = 680 kA/m	**692859-3EA**
	Sm_2Co_{17}, alloy 24, Discs 10X6 mm	$B(H)_{max}$ =190 kJ/m^3 (24 MGsOe), B_r = 1.0T (10.0kGs), H_{cb} = 740 kA/m	**692840-3EA**
	Sm_2Co_{17}, alloy 30, Discs 10X6 mm	$B(H)_{max}$ =240 kJ/m^3 (30 MGsOe), B_r = 1.16T (11.6kGs), H_{cb} = 840 kA/m	**692832-3EA**
Aluminum-Nickel-Cobalt Alloys	AlNiCo, alloy 1, Discs 13X6 mm	$B(H)_{max}$ =8.0kJ/m^3 (1 MGsOe), B_r = 0.43T (4.3kGs), H_{cb} = 30 kA/m	**692883-3EA**
	AlNiCo, alloy 5, Discs 13X6 mm	$B(H)_{max}$ =40.0kJ/m^3 (5 MGsOe), B_r = 1.25T (12.5kGs), H_{cb} = 48 kA/m	**692867-2EA**
	AlNiCo, alloy 11, Discs 13X6 mm	$B(H)_{max}$ =84.0kJ/m^3 (10.6 MGsOe), B_r = 1.12T (11.2kGs), H_{cb} = 109 kA/m	**692875-3EA**
Neodymium-Iron-Boron Alloys	NdFeB alloy 30/100, Discs 13X6 mm	$B(H)_{max}$ =239.0kJ/m^3 (30. MGsOe), B_r = 1.14T (11.4kGs), H_{cb} = 820 kA/m, Max. temp. 100 °C	**693790-5EA**
	NdFeB alloy 30/150, Discs 13X6 mm	$B(H)_{max}$ =247.0kJ/m^3 (31. MGsOe), B_r = 1.13T (11.3kGs), H_{cb} = 844 kA/m Max. temp. 150 °C	**693782-3EA**
	NdFeB, alloy 30/200, Discs 13X6 mm	$B(H)_{max}$ =248.0kJ/m^3 (31. MGsOe), B_r = 1.14T (11.4kGs), H_{cb} = 835 kA/m Max. temp. 200 °C	**693820-3EA**

$B(H)_{max}$: Maximum Energy Product; B_r: Residual Induction; Max. temp.: Maximal operation temperature; H_{cb}: Coercive force through magnetization

For more information, please visit ***sigma-aldrich.com/metals***.

Sintered **NdFeB** alloys:

- the most powerful magnets available
- manufactured by a power metallurgical process, involving the sintering of powder compacts under vacuum
- grinding and slicing possible
- low resistance to corrosion
- coating may be applied depending on the expected environment

Application: electronic devices, electric motors, engineering equipment, medical equipment

Sintered **SmCo** alloys:

- most excellent temperature characteristics in Rare Earth magnet family
- manufactured by powder metallurgical process involving the sintering of powder under vacuum
- good corrosion resistance
- no additional surface treatment required
- grinding and slicing operations possible

Applications: electronic devices, sensors, detectors, radars, and other high-tech equipment.

Cast **Alnico** alloys:

- vast range of complex shapes and sizes at an economical cost ideal for high temperature application up to 550 °C
- good corrosion resistance
- density ranging from 6.9 g/cm^3 to 7.39 g/cm^3
- a typical hardness—50 Rockwell C,
- suitable for grinding

Application: automotive applications, electronic devices, electric motors, aerospace applications, equipment.

Intermetallic Hydrides With High Dissociation Pressure




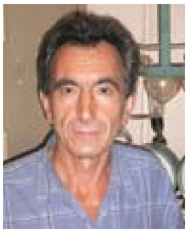

Prof. Victor N. Verbetsky, Dr. Sergey V. Mitrokhin,
Dr. Timur A. Zotov and Elshad A. Movlaev

Lomonosov Moscow State University, Russian Federation

Introduction

An initial report on the ability of alloys and intermetallics to form compounds with hydrogen dates back to 1958, when Libowitz[1] showed that ZrNi easily and reversibly reacts with hydrogen forming $ZrNiH_3$. However, the birth of a new field, chemistry of intermetallic hydrides, is usually considered to be coincident with the discovery a decade later of hydride-forming compounds such as $SmCo_5$[2] and other rare earth AB_5[3] and AB_2[4] intermetallics.

Practical applications of intermetallic hydrides are based on their chemical interaction with hydrogen. In general, this reaction may be described by the following equation:

$$M + x\,H_2 \underset{P_2,T_2}{\overset{P_1,T_1}{\Longleftrightarrow}} MH_{2x}$$

where M is a metal or an intermetallic compound. The rates of reaction for intermetallic compounds differ dramatically from those for individual metals. This peculiarity immediately brought attention to intermetallic hydrides as prospective materials for hydrogen storage and distribution. A majority of conventional materials absorb hydrogen at high rates at room temperature and low pressure. However, practical interest in these intermetallic hydrides is rather limited due to their relatively low reversible gravimetric hydrogen absorption capacity (1.4–1.9 mass.%). At the same time, in light of the greater safety of intermetallic hydrides compared to the hydrides of light metals, and the breadth of experience in applications, the development of new materials with a wide range of operating hydrogen pressures is of great practical interest. Moreover, current availability of novel high-pressure vessels (up to 250–350 atm), and development of 800 atm vessels, facilitate the investigation of high-pressure metal-hydrogen systems. Indeed, storing hydrogen in a high-pressure vessel filled with a metal hydride combines the advantages of both compressed gas and solid state hydrogen storage techniques, thus increasing total capacity of the storage container by at least 10%. The metal hydrides based systems with high hydride dissociation/hydrogen desorption pressures are also extremely attractive for applications in high-pressure compressors and internal combustion engines as a part of cold-start ignition systems.

High-Pressure Device

The interaction of intermetallic compounds with hydrogen was studied in a new high-pressure apparatus in the temperature range between 243 and 573 K. A schematic drawing of the high-pressure system is shown in **Figure 1**.

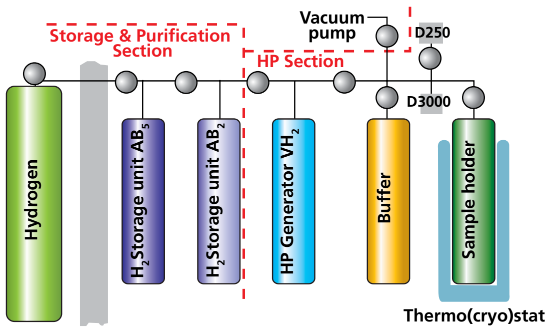

Figure 1. Schematic of a high-pressure (HP) system.

The unit consists of a section for preliminary hydrogen purification and the high-pressure (HP) section. The preliminary purification section consists of a hydrogen source vessel and two hydrogen storage and purification units—one filled with an AB_5-type alloy ($LaNi_5$, Aldrich Prod. No. **685933**) and the second containing an AB_2-type alloy ($((Ti,Zr)(V,Mn)_2$, Aldrich Prod. No. **685941**). This configuration prevents possible contamination of the HP generator system, containing vanadium hydride (VH_2), by impurities in hydrogen, which may poison the surface of VH_2, reduce its absorption capacity and, consequently, hamper its performance. The HP section consists of the HP-generator system containing VH_2, a sample holder, a buffer vessel, and two pressure transducers (D250 and D3000) with upper pressure limits of 250 and 3000 atm. Both the sample holder and the HP generator can be heated to high temperatures (up to 573 K) using muffle furnaces. The experimental temperature around the sample holder can also be maintained with a thermostat operating in the temperature range from 243K to 333 K. The data from pressure transducers and from thermocouples attached to the sample holder and the HP generator are collected by a computer-controlled data acquisition system. In order to perform correct hydrogen absorption and desorption calculations, we determined the volumes of all constituent parts of the system. These volumes were obtained in two ways—by calculations based on blueprint dimensions and by volumetric measurements after filling with water. The volume of the sample holder was found to be 8.929 mL. While calculating the total volume of the sample holder, the volume of the alloys and the relevant hydride were also taken into account. A typical sample size during our experiments varied between 15 and 20 g. The amounts of absorbed or desorbed hydrogen were calculated using a modified Van der Waals equation:[5]

$$[p+a(p)/V^{\alpha}][V-b(p)] = RT \qquad (1)$$

where, a, b = pressure dependent coefficients (for p>1 atm);
p = pressure (atm);
T = temperature (K);
V = system volume (cm^3);
R = universal gas constant (82.06 cm^3·atm/mole·K).

Thermodynamic parameters of the desorption reaction were determined using the Van't Hoff equation and fugacity values, corresponding to experimental pressure values:

$$RT\ln(f_p) = \Delta H - T\Delta S \qquad (2)$$

where, f_p = fugacity;
ΔH = enthalpy change;
ΔS = entropy change.

Finally, the fugacity values were calculated using Equation 3 and real molar volumes obtained from Equation 1:

$$RT\ln(f_p) = RT\ln p - \int_0^p (V_{id}-V_{real})dp \qquad (3),$$

where, V_{real} = real absorbed/desorbed hydrogen molar volume
V_{id} = ideal absorbed/desorbed hydrogen molar volume

It is also worth noting that our system allows for conducting experimental studies of hydrogen absorption by intermetallics as well as investigating the behavior of various materials at high hydrogen pressures.

YNi_5–H_2 System

Interaction of hydrogen with AB_5-type intermetallics at high pressures has been reported.[6] For $LaCo_5$, $La_{0.5}Ce_{0.5}Co_5$, and $LaNi_5$ it was shown that at high hydrogen pressures they form intermetallic hydrides of the approximate composition RT_5H_9 (R = rare earth metal; T = transition metal), which agrees with theoretical predictions.[6] For our studies, we chose a YNi_5 alloy because of its unique properties. YNi_5 does not easily absorb hydrogen[7–9] at low pressures. However, as shown by Takeshita[10], applying 1550 atm to the materials allows the synthesis of $YNi_5H_{3.5}$ hydride. Pressure-composition-temperature (PCT) isotherms obtained led to a conclusion that the pressure applied was not sufficient to obtain a fully hydrogenated sample. The results of other authors[11] differed considerably from that of Takeshita.

Our studies showed that an active interaction of YNi_5 and hydrogen starts at pressures over 500 atm and the equilibrium hydrogen absorption pressure at 293 K is 674 atm while corresponding equilibrium desorption pressure is 170 atm. Hydride composition at 1887 atm corresponds to YNi_5H_5 (1.3 mass.% H_2). Absorption-desorption PCT-isotherms at the temperatures ranging from –20 to 80 °C are shown in **Figure 2**. Our data differs from those reported in reference 10, where there are two desorption plateaus at 300 and 1000 atm (293 K) and the hydride composition corresponds to $YNi_5H_{3.5}$. Our data also differs from the results reported in reference 11, where the dissociation pressure is only 12 atm and the hydride composition is $YNi_5H_{4.4}$.

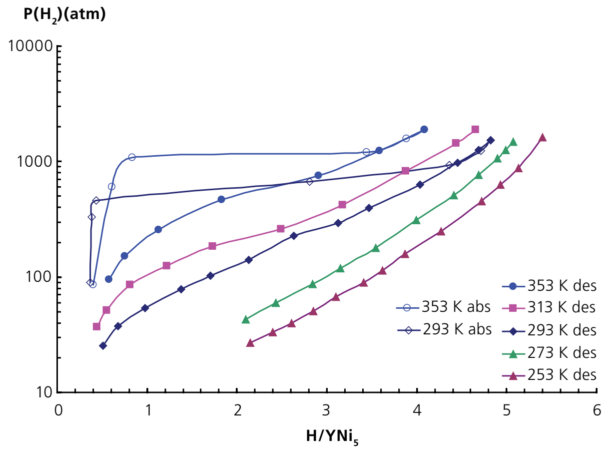

Figure 2. Absorption-desorption isotherms for YNi_5–H_2 system.

The inconsistency in the numbers reported by different groups may be explained by very low hydrogen absorption and desorption rates observed. In our case, the time to reach equilibrium in the plateau region was between 2 and 4 hours; see **Figure 3** which shows the readings of the pressure transducer in several consecutive hydrogen desorption steps.

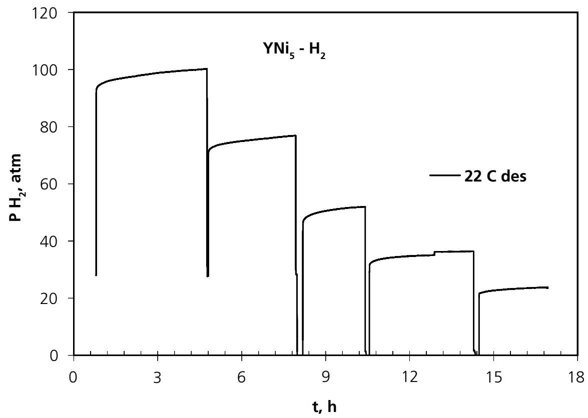

Figure 3. Dependence of pressure change (P) on time (t) to equilibrium.

A number of authors[7–9] compared hydrogen absorption properties of YNi_5 to other AB_5 alloys and concluded that peculiarities in its interaction with hydrogen can be explained neither by the low-temperature heat capacity nor the electronic structure, nor by the surface oxidation of YNi_5. In our opinion, the most possible explanation was given in reference 8, where it was shown that among all binary AB_5-type intermetallic compounds YNi_5 has the lowest compressibility. Thus, the low volume of the YNi_5 unit cell could influence hydrogen absorption properties.

Using a $\ln P(H_2)$ vs. 1/T plot, we found the values of hydrogen desorption enthalpy and entropy of a YNi_5 hydride to be 21.86 kJ/mol H_2 and 115.8 J/K·mol H_2 respectively.

AB_2–H_2 Systems

As basis materials for these studies, we selected Laves phases $ZrFe_2$ and $TiFe_2$ with high hydrogen desorption pressures, which do not absorb hydrogen at relatively low pressures. It has been reported that using the ultra-high pressure of 10,000 atm, it is possible to synthesise a $ZrFe_2$ hydride.[12–14] Our studies showed that noticeable hydrogen absorption in the first absorption-desorption cycle starts at approximately 800 atm without any preliminary activation. During subsequent cycling, absorption starts at lower pressures. Absorption equilibrium pressure in the first run has been found to be 1120 atm while in second and further cycles it decreased to 690 atm (**Figure 4**). The hydrogen content in the hydrogenated material at room temperature and 1800 atm is 3.5 H/formula unit. At the low temperature of 218 K and hydrogen pressure of 1900 atm, the material's composition is $ZrFe_2H_{3.7}$. The isotherms shown in Figure 4 reveal an obvious hysteresis—at room temperature the absorption equilibrium pressure is about 690 atm, while the desorption one is only 325 atm.

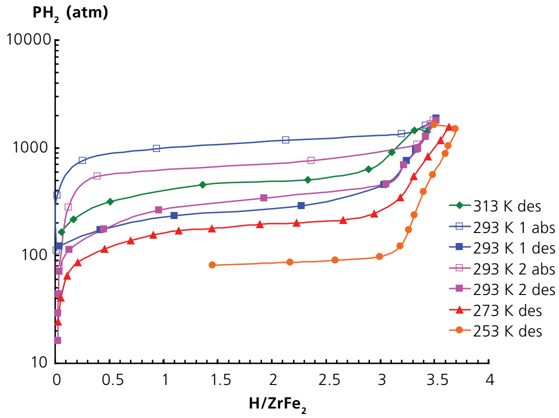

Figure 4. Absorption-desorption isotherms for $ZrFe_2$–H_2 system.

Partial substitution of zirconium for scandium reduces the hydrogen desorption pressure of the hydride. Similar to $ZrFe_2$, $Zr_{0.5}Sc_{0.5}Fe_2$ and $Zr_{0.8}Sc_{0.2}Fe_2$ crystallize as C15 Laves phases. Hydrogen absorption in $Zr_{0.5}Sc_{0.5}Fe_2$ starts at ~100 atm without any preliminary activation. There is no significant hysteresis in this system, i.e. the absorption and desorption pressures are very close. Hydrogen content in the material at 295 K and 1560 atm reaches 3.6 H/formula unit (**Figure 5**).

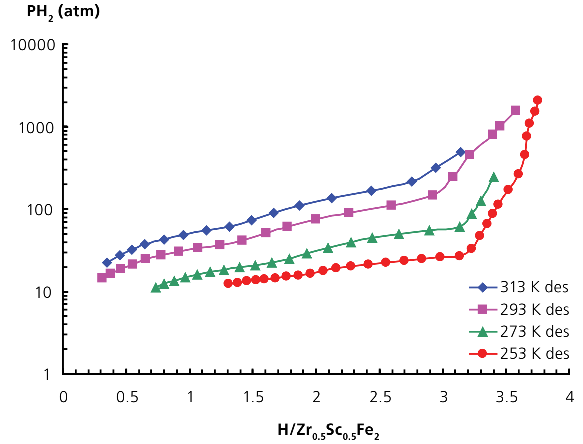

Figure 5. Absorption-desorption isotherms for $Zr_{0.8}Sc_{0.2}Fe_2$–H_2 system.

The shape of the hydrogen absorption-desorption isotherms suggests the formation of two hydride phases in the $Zr_{0.5}Sc_{0.5}Fe_2$–H_2 system. At room temperature, the composition of the first phase (β1) is close to a dihydride and that of the second one (β2) corresponds to a trihydride (**Table 1**). Hydrogen desorption enthalpies and entropies have been calculated for both phases. Remarkably, the behavior of $Zr_{0.5}Sc_{0.5}Fe_2$ resembles that of the $ScFe_{1.8}$–H_2 system, where the stable monohydride and the much less stable $ScFe_{1.8}H_{2.4}$ are also formed.[15,16] In our case, however, substitution of half of the scandium for zirconium leads to a significant increase of stability of the lower hydride with an enthalpy of formation lower than that of the trihydride (Table 1).

Table 1. Thermodynamic parameters for $Zr_{1-x}Sc_xFe_2$–H_2 systems.

IMC*	H/IMC	P_{des}, atm	T, K	f_{des}**, atm	ΔH, kJ/moleH$_2$/ ΔS, J/K·moleH$_2$
$ZrFe_2$	2.0	86	253.1	90.5	21.3(3) / 121(1)
		170	273	188	
		325.1	295.7	396.7	
		468.8	313	619	
$Zr_{0.5}Sc_{0.5}Fe_2$	1.3	12.5	254.1	12.5	19(2) / 95(6)
		18.7	272.6	18.7	
		38.8	295.1	39.7	
		60.5	310.9	62.5	
	2.5	22	254.1	22	25.4(4) / 125(1)
		46.4	272.6	47.4	
		105	295.1	111.5	
		177	310.9	195.5	
$Zr_{0.8}Sc_{0.2}Fe_2$	1.8	49	253.4	50	21(1) / 117(5)
		190	292.1	212	
		290	313.1	343	

*Intermetallic compound
**Fugacity

Comparing hydrides $ScFe_{1.8}H_{1.8}$, $Zr_{0.5}Sc_{0.5}Fe_2H_{2.5}$ (second plateau) and $Zr_{0.8}Sc_{0.2}Fe_2H_{1.8}$ shows that the increase in zirconium content in the alloys leads to the decrease in its hydrogen desorption enthalpy. However, entropy change goes through a maximum at $Zr_{0.5}Sc_{0.5}Fe_2H_{2.5}$ (Table 1).

For $Zr_{0.8}Sc_{0.2}Fe_2$–H_2, hydrogen absorption also starts at 100 atm without activation. Hydrogen composition at room temperature (293K) and 1650 atm is $Zr_{0.8}Sc_{0.2}Fe_2H_{3.7}$ (**Figure 6**). Further cooling to 219 K with simultaneous increase in hydrogen pressure to 1730 atm results in maximum hydride composition corresponding to $Zr_{0.8}Sc_{0.2}Fe_2H_{3.8}$.

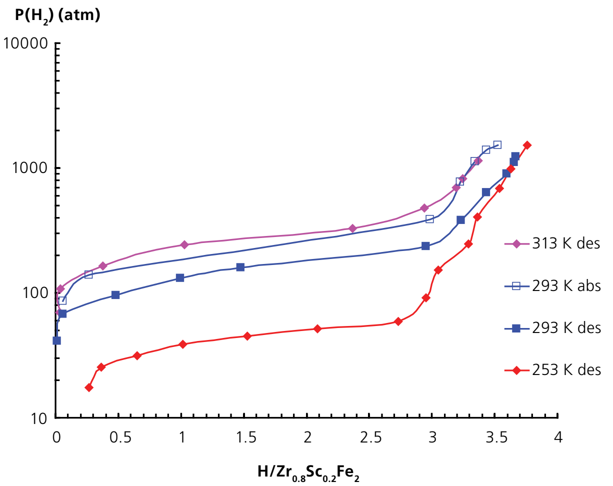

Figure 6. Desorption isotherms for $Zr_{0.5}Sc_{0.5}Fe_2$–H_2 system.

Partial substitution of titanium for scandium allowed us to synthesize the first pseudobinary intermetallic hydride in $Ti_{0.5}Sc_{0.5}Fe_2$–H_2 system. Remarkably, while $Ti_{0.8}Sc_{0.2}Fe_2$ does not absorb hydrogen even at pressures up to 2500 atm, at 223 K, the reaction between $Ti_{0.5}Sc_{0.5}Fe_2$ and hydrogen starts at room temperature already at 100 atm without any preliminary activation (**Figure 7**). The hydrogen content of the hydride corresponds to $Ti_{0.5}Sc_{0.5}Fe_2H_{3.1}$ (2.0 mass%).

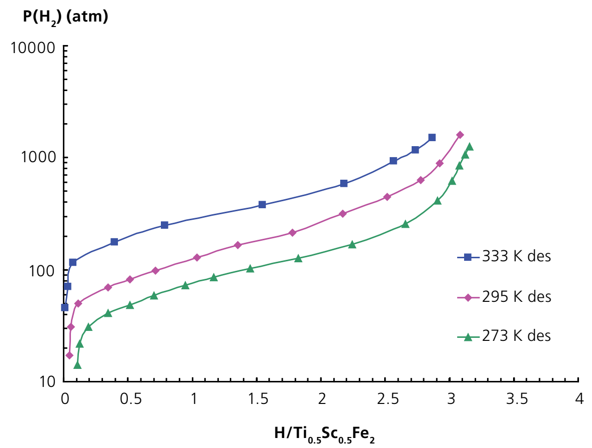

Figure 7. Desorption isotherms for $Ti_{0.5}Sc_{0.5}Fe_2$–H_2 system

The room temperature equilibrium absorption and desorption pressures for this material are 195 and 175 atm accordingly. Cooling the hydrogenated material to below 223 K showed that no new hydride phase transition occurs. Hydrogen content at 217 K at 2700 atm is 3.4 H/f.u. (2.16 mass.%) and calculated thermodynamic parameters were are ΔH (kJ/moleH2) = 17.7(2) and ΔS (J/K· moleH2) = 103.8(7)

Conclusions

Interaction of hydrogen with multi-component intermetallic compounds of AB5- and AB2-type were studied in the current work. Several new intermetallic hydrides with potential applications in high-capacity hydrogen storage have been identified and fully characterized using a gas-volumetric analytical technique.

Acknowledgements

This work was supported in part by General Motors Corp.

References:

(1) Libowitz G. G.; Hayes H. F.; Gibb T. R. P. *J. Phys. Chem.* **1958**, *62*, 76. (2) Zijlstra H.; Westendorp F. F. *Solid State Comm.* **1969**, *7*, 857. (3) van Vucht J. H. N.; Kuijpers F. A.; Bruning H. C. A. M. *Philips Research Reports* **1970**, *25*, 133. (4) Pebler A.; Gulbransen. E. A. *Trans. Met. Soc. AIME* **1967**, *239*, 1593. (5) Hemmes H.; Driessen A.; Griessen R. *J. Phys. C* **1986**, *19*, 3571. (6) Lakner J. F.; Uribe F.; Steward S. A. *J. Less-Common Met.* **1980**, *72*, 87. (7) Takeshita T.; Gschneidner K. A. Jr.; Thome D. K.; McMasters O. D. *Physical Review B* **1980**. *21*, 5636. (8) Takeshita T.; Wallace W. E.; Craig R. S. *Inorg. Chem.* **1974**, *13*, 2282. (9) Sarynin V. K.; Burnasheva V. V.; Semenenko K. N. *Izvestiya AN SSSR, Metally*, **1977**, *4*, 69. (10) Takeshita T.; Gschneidner K. A. Jr.; Lakner J. F. *J. Less-Common Met.* **1981**, *78*, 43. (11) Anderson J. L.; Wallace T. C.; Bowman A. L.; Radosewich C. L.; Courtney M. L. *Los Alamos Rep.LA-5320-MS, Informal Report*, **1973**. (12) Filipek S. M.; Jacob I.; Paul-Boncour V.; Percheron-Guegan A.; Marchuk I.; Mogilyanski D.; Pielaszek J. *Polish Journal of Chemistry* **2001**, *75*, 1921. (13) Filipek S. M.; Paul-Boncour V.; Percheron-Guegan A.; Jacob I.; Marchuk I.; Dorogova M.; Hirata T.; Kaszkur Z. *J. Phys.: Condens. Matter.* **2002**, *14*, 11261. (14) Paul-Boncour V.; Bouree-Vigneron F.; Filipek S. M.; Marchuk I.; Jacob I.; Percheron-Guegan A. *J. Alloys Compds.* **2003**, *356–357*, 69. (15) Semenenko K. N.; Sirotina R. A.; Savchenkova A. P.; Burnasheva V. V.; Lototskii M. V.; Fokina E. E.; Troitskaya S. L.; Fokin V. N. *J. Less-Common Met.* **1985**, *106*, 349. (16) Savchenkova A. P.; Sirotina R. A.; Burnasheva V. V.; Kudryavtseva N. S. *Sov. Neorgan. Materialy* **1984**, *20*, 1507.

Hydrogen Absorbing Alloys

Name	Chem. Composition	Hydrogen Storage Capacity wt.%	Equilibrium Pressure Plateau	Prod. No.
Zirconium-Iron Alloy	$ZeFe_2$	1.65–1.75 (25 °C, 1800 bar)	~690 bar (23 °C) absorption ~325 bar (23 °C) desorption	**693812-1G**
Zirconium-Iron Alloy	$Zr_{0.8}Sc_{0.2}Fe_2$	1.65–1.75 (22 °C, 1560 bar)	~190 bar (20 °C)	**693804-1G**
Yttrium Nickel Alloy	YNi_5	1.25–1.3 (25 °C, 1890 bar)	~674 bar (20 °C)	**693928-5G**
Lanthanum Nickel Alloy	$LaNi_5$	1.5–1.6 (25 °C)	~2 bar (25 °C)	**685933-10G**
Lanthanum Nickel Alloy	$LaNi_{4.5}Co_{0.5}$	1.4–1.5 (25 °C)	<0.5 bar (25 °C)	**685968-10G**
Mischmetal Nickel Alloy	$(Ce, La, Nd, Pr)Ni_5$ Ce: 48–56%; La: 20–27%; Nd: 12–20%;Pr : 4–7%	1.5–1.6 (25 °C)	~10 bar (25 °C)	**685976-10G**
Titanium Manganese Alloy 5800	$Ti_{0.98}Zr_{0.02}V_{0.43}Fe_{0.09}Cr_{0.05}Mn_{1.5}$	1.6–1.7 (25 °C)	~10 bar (25 °C)	**685941-10G**

For more information about these and related materials, please visit ***sigma-aldrich.com/hydrogen***.

High-Purity Iron, Nickel, Titanium and Zirconium

Metal	Physical Form	Size/Dimensions	Purity, %	Prod. No. & Avail. Pkg. Size
Iron (Fe)	Chips		99.98	**267945** (250 g, 1 kg)
	Granules	10–40 mesh	99.999	**413054** (5 g, 25 g)
	Rod	diam. 6.3 mm	99.98	**266213** (30 g, 150 g)
	Powder	Reduced	≥99.0	**44900** (50 g, 250 g, 1 kg)
		fine powder	99.99+	**255637** (10 g, 50 g)
		<150 µm	≥99	**12312** (250 g, 1 kg, 6 x 1 kg)
		<10 µm	99.9+	**267953** (5 g, 250 g, 1 kg)
Nickel (Ni)	Rod	diam. 6.35 mm	99.99+	**267074** (14 g, 42 g)
	Powder	<150 µm	99.999	**266965** (50 g)
		<150 µm	99.99	**203904** (25 g, 100 g, 500 g)
		3 µm	99.7	**266981** (100 g, 500 g)
		<1 µm	99.8	**268283** (25 g, 100 g)
Titanium (Ti)	Crystalline	5–10 mm	99.99+excl. Na and K	**305812** (25 g, 100 g)
	Rod	diam. 6.35 mm	99.99	**347132** (7.2 g, 36 g)
	Powder	–325 mesh	99.98	**366994** (10 g, 50 g)
Zirconium (Zr)	Crystal bar, turnings		99.9+	**497428** (100 g)
	Sponge		≥99.0	**267651** (100 g, 500 g)
	Rod	diam. 6.35 mm	≥99.0	**267724** (20 g, 100 g)
	Wire	diam. 0.127 mm	99.95	**267694** (80 mg)

For more information about these and other related materials, please visit ***sigma-aldrich.com/metals***.

Pure Metals from Sigma-Aldrich

Alkali Metals	Alkali Earth Metals	Transition Metals	Main Group Metals	Rare Earth Metals	Radioactive Elements

Li 62360, 62358, 248827, 499811, 444456, 265977, 266000, 265993, 320080, 265985, 265969, 220914 278327, 340421, 601535	**Be** 265063, 459992, 378135						
Na 483745, 262714, 282057, 282065, 597821, 244686, 71172	**Mg** 13110, 63037, 13112, 254118, 474754, 465992, 466018, 254126, 253987, 465666, 368938, 380628 266302, 299405, 403148, 200905						
K 244856, 244864, 60030, 12621, 679909	**Ca** 441872, 596566, 215147, 327387, 215414, 12001	**Sc** 261246, 261262	**Ti** 267503, 460397, 348791, 348813, 348848, 578347, 268496, 366994, 513415, 347132, 266051, 268526, 348856, 267902, 348864, 460400, 266019	**V** 467286, 266191, 357162, 357170, 266205, 262935, 266175, 262927	**Cr** 12221, 374849, 255610, 229563, 266264, 266299	**Mn** 266167, 266159, 266132, 463728	**Fe** 44890, 00631, 12312, 44900, 12311, 267945, 413054, 338141, 356808, 513423, 255637, 209309, 267953, 266213, 266256, 356824, 356832
Rb 276332, 385999	**Sr** 441899, 460346, 474746, 403326, 343730	**Y** 451347, 261319, 261327	**Zr** 497428, 267678, 419141, 403288, 403296, 267724, 267651, 369470	**Nb** 262781, 262803, 268488, 262749, 262722, 593257, 265489, 262765, 262730	**Mo** 357200, 357219, 266930, 266922, 514802, 357227, 203823, 266892, 366986, 510092, 577987, 266949, 266914, 266906	**Tc**	**Ru** 545023, 209694, 267406
Cs 14714, 239240	**Ba** 474711, 441880, 474738, 595101, 403334, 237094	**La** 61451, 263117, 261130, 263109	**Hf** 266795, 356905, 266787, 266752, 266760, 266809, 266779	**Ta** 262889, 357251, 262897, 357243, 262919, 545007, 262846, 593486, 262854, 262862, 357006	**W** 357189, 67546, 357197, 267538, 267511, 357421, 510106, 577294, 276324, 267562, 267554, 356972	**Re** 267317, 267295, 267309, 204188, 267279, 449482, 357138, 267287	**Os** 263257, 327409

▸ *For more available products in this category, please visit our Web site.*

Ce 461210, 261041, 263001	**Pr** 263176	**Nd** 261157, 460877	**Pm**	**Sm** 84433, 261211, 263184, 261203	**Eu** 457965, 261092

Product numbers in the metallic element cells of the periodic table reflect the variety of forms and sizes available.
Visit ***sigma-aldrich.com/metals*** for details.

				Al 13103, 63034, 63045, 63035, 11010, 11009, 424803, 433713, 433705, 518573, 266957, 266574, 326852, 326860, 356859, 326941, 338788, 202584, 214752, 266515, 653608, 202576, 266523		
Co 12930, 356891, 266671, 356867, 203076, 266655, 266647, 266639, 266701, 398810	**Ni** 357553, 267007, 268259, 357588, 266965, 203904, 266981, 268283, 577995, 267074, 215775, 267058, 357626, 357634	**Cu** 61139, 61141, 12806, 12816, 326445, 266744, 349151, 349178, 349208, 311405, 203122, 266086, 207780, 326453, 357456, 292583, 634220, 65327, 254177, 326488, 223409, 520381, 349224	**Zn** 31653, 14401, 14406, 14409, 14409, 05603, 209988, 349410, 267619, 356018, 565148, 266345, 243469, 243477, 215503, 215481, 266353, 24930, 578002, 267635, 402583, 266361, 267929	**Ga** 203319, 263273, 263265	**Ge** 263230, 203343, 327395, 203351	
Rh 267376, 357340, 204218	**Pd** 373206, 287474, 348643, 267139, 411450, 267120, 203998, 203939, 464651, 326658, 326666, 346993, 267082, 267112, 348694, 326690, 348708	**Ag** 373249, 327077, 267457, 326976, 348724, 369438, 265543, 265535, 345075, 348716, 326984, 267449, 265527, 326992, 348740, 265519, 03372, 461032, 265500, 327107, 327093, 327085, 484059	**Cd** 265411, 265330, 414891, 265365, 265357, 265454, 202886, 385387, 265403, 348600	**In** 57083, 264113, 357278, 326631, 357286, 357294, 264040, 264059, 357308, 326615, 203432, 264032, 277959, 264091, 326607, 357065, 278319, 340863, 357073, 264075, 264067, 357081, 326623	**Sn** 14509, 14507, 14511, 96523, 265659, 265756, 356948, 243434, 265667, 265640, 265632, 520373, 576883, 204692, 217697, 356956	**Sb** 452343, 264830, 266329, 266604
Ir 449229, 357332, 266833, 357324, 209686, 266825, 357103, 266841, 336793	**Pt** 373214, 373222, 373230, 349372, 267260, 305189, 349321, 327425, 349348, 327433, 267252, 349380, 349356, 303798, 349364, 267244, 298107, 298093, 204048, 204013, 327441, 327476, 327484	**Au** 326542, 373168, 373176, 373184, 265829, 326518, 349240, 326496, 265810, 349259, 349275, 268461, 349267, 326593, 255734, 265772, 326585, 636347, 265837, 289779, 265802, 349291, 349305	**Hg** 83359, 83360, 294594, 215457, 261017	**Tl** 277932	**Pb** 265934, 396117, 265918, 356913, 243485, 11502, 369748, 391352, 209708, 265853, 265861, 357014, 265888, 357235, 356921	**Bi** 556130, 202819, 95372, 264008, 265462, 452386, 265470

Gd 263087, 261114, 263060	**Tb** 263206	**Dy** 263028, 261076, 263036	**Ho** 457957, 261122	**Er** 263052, 261084, 263044	**Tm** 261289, 263222	**Yb** 262986, 548804, 261300, 466069, 261297	**Lu** 261149

Lightweight Metal Matrix Nanocomposites — *Stretching the Boundaries of Metals*

Prof. P. K. Rohatgi and B. Schultz

University of Wisconsin–Milwaukee

Introduction

Composite materials that traditionally incorporate micron scale reinforcements in a bulk matrix offer opportunities to tailor material properties such as hardness, tensile strength, ductility, density, thermal and electrical conductivity, and wear resistance. With the advent of nanomaterials, nanocomposites are envisioned, and are being developed, with properties that overcome the limitations for metals or composites that contain micron scale reinforcements. For example, carbon nanotubes have been shown to exhibit ultra-high strength and modulus, and have anisotropic electrical conductivity. When included in a matrix, carbon nanotubes could impart significant property improvements to the resulting nanocomposite.[1]

In the past decade, much work has gone towards developing polymer matrix nanocomposites and many such materials are already used in various applications.[2] Metallic composites containing nanoparticles or carbon nanotubes could offer distinct advantages over polymeric composites due to the inherent high temperature stability, high strength, high modulus, wear resistance, and thermal and electrical conductivity of the metal matrix. Aluminum nanocomposites are predicted to surpass the weight reduction currently realized through the use of polymer-based nanocomposites and polymer-based fiber composites in aerospace applications primarily because these metal matrices have higher strength and stiffness (**Figure 1**). They also have much better thermal stability.

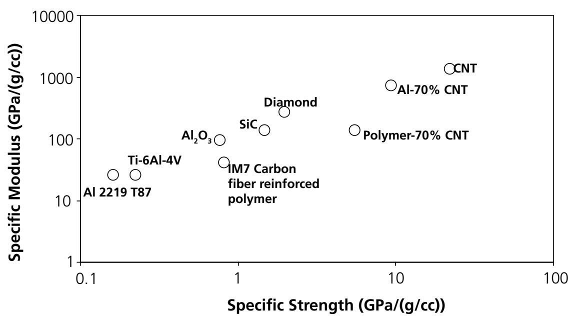

Figure 1. Comparison of potential materials and reinforcements for aerospace applications. (Data for Al-70% CNT is theoretical)

The development of Metal Matrix Nanocomposites (MMNCs), however, is still in its infancy. The MMNCs synthesized to date include Al-B_4C, Mg-SiC, Al-CNT, Cu-CNT and Ti-SiC, prepared using powder metallurgy, and Al-SiC, Mg-SiC, Al-Al_2O_3, Al-CNT, Mg-Y_2O_3, Al-Diamond, and Zn-SiC, prepared using solidification processing.

Though there is great potential for the use of MMNCs in a variety of applications, their use is hindered by their cost, difficulty in the manufacture of large complex shaped parts and their often poor ductility. This article briefly reviews the state-of-the-art in metal matrix nanocomposites, with specific emphasis on how these drawbacks are being overcome through proactive design of nanostructures and processing techniques.

Synthesis, Processing and Properties of Metal Matrix Nanocomposites

The greatest challenges facing the development of MMNCs for wide application are the cost of nanoscale reinforcements and the cost and complexity of synthesis and processing of nanocomposites using current methods. As with conventional metal matrix composites with micron-scale reinforcements, the mechanical properties of a MMNC are strongly dependent on the properties of reinforcements, distribution, and volume fraction of the reinforcement, as well as the interfacial strength between the reinforcement and the matrix. Due to their high surface area, nanosize powders and nanotubes will naturally tend to agglomerate to reduce their overall surface energy, making it difficult to obtain a uniform dispersion by most conventional processing methods. In addition, due to their high surface area and surface dominant characteristics, these materials may also be highly reactive in metal matrices. For example, in Al/CNT composites there are concerns that brittle aluminum carbide phases could form during processing, impairing the mechanical properties and electrical conductivity of the nanocomposite. Because of these concerns, processing methods are being developed to produce MMNCs with uniform dispersions of nanomaterials and little deleterious interfacial reactions.

The methods that have been used to synthesize metal matrix nanocomposites include powder metallurgy, deformation processing, vapor phase processing, and in some cases solidification processing. Powder metallurgy involves the preparation of blends of powders of metal and reinforcements, followed by consolidation and sintering of the mixtures of powders to form the part. Deformation processing involves subjecting a metal to high rates of deformation to create nanostructured grains in a metal matrix. Vapor phase processing methods such as chemical vapor deposition (CVD) can be used to deposit thin films creating dispersed multiphase microstructures, multilayered microstructures, or homogeneous nanostructured coatings. Each of these methods can create very desirable microstructures, however they are expensive and difficult to scale up to manufacture large and complex shapes in bulk.

Of the processing methods available for synthesis and processing of MMNCs, the least expensive method for production of materials in bulk is solidification processing. There are various avenues by which researchers have created nanostructures and nanocomposite materials using solidification and these can be divided into three categories 1) rapid solidification, 2) mixing of nanosize reinforcements in the liquid followed by solidification and 3) infiltration of liquid into a preform of reinforcement followed by solidification. Rapid solidification (implying solidification rates of up to 10^4–10^7 °C/s) through methods such as melt spinning (a liquid metal stream is impinged on a spinning copper drum), or spray atomization (a superheated liquid metal is atomized with gas jets and impinged on a substrate) can lead to nanosize grains as well as amorphous metals from which nanosize reinforcements can be precipitated in the amorphous matrix during heating to form nanocomposites.[3,4] Mixing techniques involve adding particulate reinforcements and mechanically dispersing them in the matrix. Mixing methods that have been applied to synthesize MMNCs include stir mixing, where a high temperature impeller is used to stir a melt that contains reinforcements, creating a vortex in the melt, and ultrasonic mixing, where an ultrasonic horn is used to create cavitation in the melt that disperses the particulate reinforcements by a gas streaming effect that occurs through the collapse of bubbles within the melt. Infiltration techniques entail infiltrating a preform or partial matrix containing the reinforcements with a liquid metal. The preform consists of particles formed in a particular shape with some binding agent, and can be composed of the additives and binding agent alone or with some portion of the matrix added as a partial filler. Infiltration methods that have been used include ultra high pressure, where the pressure used to infiltrate a high-density preform of nanoparticles is in excess of 1 Gpa, and pressureless infiltration, where a block of metal is melted on top of a lower density preform of nanoparticles and allowed to seep into the preform.[5,6]

Figure 2 illustrates examples of the different microstructures of Aluminum Alloy-Al_2O_3 nanoparticle (Aldrich Prod. No. **544833**) composites that have been produced by different processing methods. **Figure 2A** shows a microstructure exhibited by a cast nanocomposite synthesized at UW–Milwaukee by the authors. This MMNC was made using a unique casting method combining the use of stir mixing, and ultrasonic mixing, with a wetting agent added to the molten alloy to incorporate nanoparticles in a metal matrix. This process resulted in the incorporation of nanoparticles within microscale grains of aluminum, and formed a bimodal microstructure. Ceramic nanoparticles may be uniformly dispersed in metal matrices to increase the tensile strength and wear resistance, using methods such as ultrasonic cavitation of the melt to further disperse the particles.[7] The influence of nanoscale reinforcements on formation of solidification microstructure including their influence on nucleation, growth, particle pushing, solute redistribution, heat and fluid flow, however, will have to be understood to reproducibly create desired structures. While there is some understanding of the influence of micron size particles on the formation of solidification microstructures, the influence of nanoscale reinforcements on each of the constituents of solidification structure formation need to be studied using both theoretical and experimental research. **Figure 2B** shows a transmission electron microscope (TEM) micrograph of the microstructure obtained by ball milling pure metals and nanopowders, followed by hot pressing/sintering to form a nanocomposite. The matrix aluminum and the Al_2O_3 powders are nanosize in this TEM micrograph and the reinforcement phases are mainly restricted to the grain boundaries, which will likely have a grain boundary pinning effect. Since a much higher percentage of Al_2O_3 has been added using this process, the resulting sample exhibited a substantial improvement in its wear properties.

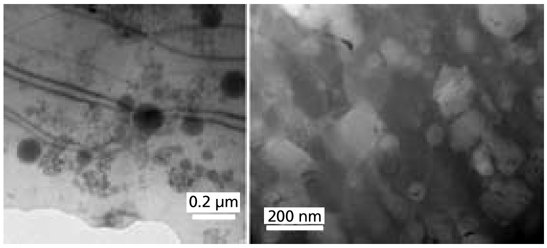

A) B)

Figure 2. TEM of Aluminum Alloy-Al_2O_3 nanocomposites produced by liquid and solid based methods. A) Stir cast A206- 2 vol % Al_2O_3 (47 nm) nanocomposite produced by the authors at UW–Milwaukee.[7] B) Powder metallurgy based Aluminum alloy-15 vol% Al_2O_3.[8]

Great improvements can be achieved in specific material properties by adding only a small percentage of a dispersed nano-phase as reinforcement. **Table 1** presents selected studies on MMNCs, the processing techniques used and their respective properties. When the reinforcement in a metal matrix is brought down from micron-scale to nano-scale, the mechanical properties are often substantially improved over what could be achieved using micron-scale reinforcements. This is possibly due to the exceptional properties of the individual nano-phase reinforcements themselves, smaller means free path between neighboring nanoparticles and the greater constraint provided by the higher surface area of nano-phase reinforcements. Nano-phase reinforcements like CNT and SiC (Aldrich Prod. No. **594911**) have much higher strengths than similar micron-scale reinforcements. In some cases, the nanoscale reinforcement leads to property changes in the matrix itself. For instance, nanoscale reinforcements can lead to nanosize grains in the matrix, which will increase the strength of the matrix. Due to their size, properties of nanomaterials are dominated by their surface characteristics, rather than their bulk properties, which is the case in micron-scale reinforcements. The potentially unique interfaces between nanosized reinforcements and the matrix can lead to even greater improvements in the mechanical properties due to the strong interface between the reinforcement phase and the matrix, and through secondary strengthening effects such as dislocation strengthening. **Figure 3** shows that as the particle size of Al_2O_3 goes from micron to nanosize, there is significant decrease in the friction coefficient and wear rate of aluminum composites. In addition, the incorporation of only 10 volume percent of 50 nm sized Al_2O_3 particles to the aluminum alloy matrix resulted in an increase of the yield strength to 515 MPa.[8] This is 15 times stronger than the base alloy, 6 times stronger than the base alloy with 46 volume percentage of 29 micron size Al_2O_3 and over 1.5 times stronger than AISI 304 stainless steel.

Table 1. Selected studies of Metal Matrix-Nanoparticle and Nanotube Composites.[7]

Team	Process	Properties and Comments
Takagi et al.[9]	Rapidly solidified nanocrystalline Al alloys and Al/SiC nanocomposites (Matrix: Al-Ni-Y-Co, Al-Si-Ni-Ce, and Al-Fe-Ti-Me, where Me: Cr, Mo, V, Zr). SiC size: #3000 to #8000	High hardness, strength and excellent wear resistance to 473 K.
El-Eskandarany[10]	High-energy ball milling of Al-SiC (2–10%) nanocomposite and consolidation using plasma activated sintering.	Fully dense bulk nanocomposites with nanocrystalline structure and uniform SiC distribution. No reaction products (Al_4C_3) or Si at the interface. Hardness and mechanical strength characterized.
Hong et al.[11]	Deformation processing (drawing) of Cu/Nb filament nanocomposites.	At drawing strain above 10, a limiting thickness of Nb filaments of 10 nm was obtained (further deformation caused filament rupture rather than thinning). The ductility was independent of the Nb content.
Islamgaliev et al.[12]	Cu-0.5wt% Al_2O_3 nanocomposites produced by high-pressure torsion technique.	High tensile strength (680 MPa) and microhardness (2300 MPa), as well as high thermal stability, creep strength and electrical conductivity were obtained.
Fekel & Mordike[13]	Mg strengthened by 30 nm-SiC particles. Nano-SiC formed by CO_2 laser-induced reaction of Si and acetylene. Micron-size Mg powder formed by gas atomization of Mg melt with Ar gas. Composite formed by hot milling followed by hot extrusion.	Tensile Strength doubled as compared to unreinforced Mg. At room temperature increase in the UTS was around 1.5 times. Significant improvement in the hardness. Milled composites exhibited lowest creep rate.
Dong et al.[14]	CNT/Cu composite. CNT formed by thermal decomposition of acetylene. CNT mixed with Cu powder using ball mill. Ball-powder weight ratio 6:1. Pressed at 350 MPa for 5 min. Sintered for 2 h at 850 °C.	Friction coefficient reduced with increasing CNT fraction in Cu. Less wear loss with increasing CNT content. Less wear loss in Cu/CNT than Cu/C as load increased.

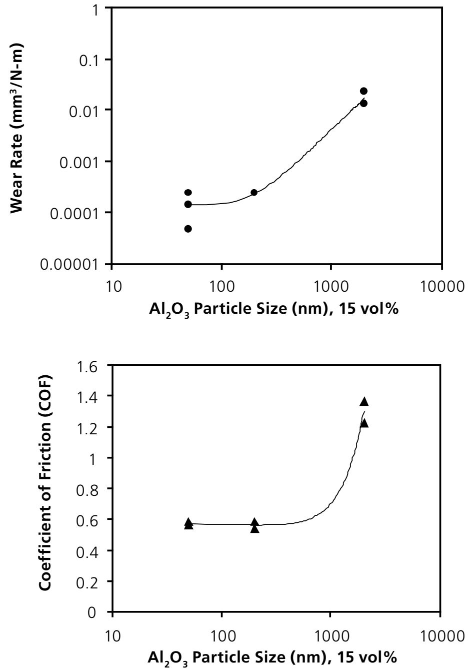

Figure 3. Effect of particle size on wear rate and coefficient of friction of Al-15vol% Al_2O_3 metal matrix composites. Both the wear rate and coefficient of friction are dramatically reduced when the particle size is reduced below 1 µm.[8]

Recently, an aluminum alloy specimen reinforced with CNTs was synthesized using pressureless infiltration.[6] CNTs were mixed together with aluminum and magnesium powders using ball milling and then pressed into preforms that were subsequently infiltrated by melts of the aluminum alloy matrix at 800 °C in a nitrogen atmosphere. The CNTs were observed to be well-dispersed and embedded in the matrix. Further experiments showed that up to 20 volume percent of nanotubes could be incorporated in the matrix of aluminum alloys using this process. The wear data also suggests that the presence of CNTs in the matrix can reduce the direct contact between the aluminum matrix and the steel pin and thereby decrease the friction coefficient due to the presence of carbon nanotubes. By reducing the friction coefficient, the energy loss experienced by components in frictional contact will be reduced, improving efficiency of mechanical systems. In addition, the authors believe that the incorporation of CNTs having relatively short tube lengths may allow them to slide and roll between the mating surfaces and result in a decrease of the friction coefficient.[6] Ploughing wear appeared to be the dominant wear mechanism under the dry sliding condition. The depth of the wear grooves caused by ploughing wear decreased with increasing CNT content, suggesting that the strengthening effects of nanotubes increased the wear resistance of aluminum alloy-CNT nanocomposite.

Though nanocomposite materials exhibit ultra high-strength, there is often a trade-off that results in decreased ductility. This may be attributed to currently used processing methods that result in the formation of voids and defects, as well as to the inability of nanostructured grains or additives to sustain a high rate of strain hardening. These shortcomings, among other microstructural effects, lead to instabilities upon plastic deformation. One of the methods that has been used to overcome the lack of ductility in nanostructured materials is to incorporate nanosize dispersoids in a bimodal or trimodal microstructure. In the case of nanostructured grains, the presence of hard precipitates or nanoparticles in a metal matrix may act to initiate, drag and pin dislocations, reducing dynamic recovery, and thus resulting in a high strain-hardening rate that, in turn, produces larger uniform strains and higher strengths in the MMNC, along with higher ductility.[15]

The potential for achieving much higher strengths in combination with acceptable ductility in MMNCs has been demonstrated by E. Lavernia and coworkers.[16] A mixture of a 5083 aluminum alloy powder and micron-sized boron carbide particles that had been coated with a powdered, nanostructured aluminum alloy were milled at cryogenic temperatures (cryomilled). This cryomilled powder was then mixed with regular 5083 alloy and consolidated and extruded to form nanocomposites with almost double the strength of the monolithic 5083 alloy. Cigar-shaped nanocomposite volumes of material that contained micron-sized B_4C reinforcements were observed to be dispersed in nano-grain sized aluminum matrix regions that were embedded in micro-grain sized 5083 aluminum matrix having no B_4C reinforcements. This combined bimodal and trimodal microstructure (**Figure 4**) is presumed to be the source of the exceptional combination of strength and ductility in aluminum matrix nanocomposites that had micron size B_4C particles used as reinforcements. Apparently, the micron grain-sized aluminum matrix that did not contain any reinforcement, enabled dislocation motion and improved ductility. This type of combined bimodal and trimodal microstructure in MMNCs will need to be synthesized using less expensive solidification processing routes that can enable processing of large components having complex shapes. By exploring lower cost and more versatile methods to manufacture metal matrix nanocomposites with improved ductility, these materials are expected to become commercially viable for a variety of applications, particularly where weight savings is essential.

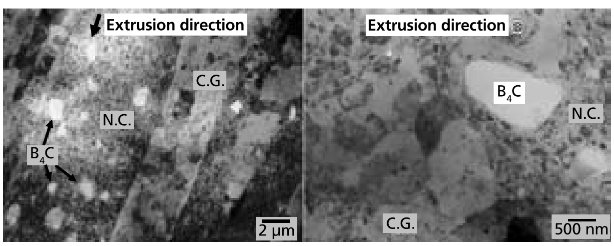

Figure 4. TEM micrographs showing alternate stacking of course grain size Al and nanostructured Al regions. The B_4C particles are uniformly distributed within the nanostructured aluminum exclusively.[16]

Current and Future Applications

Metal matrix composites with micron-size reinforcements have been used with outstanding success in the automotive and aerospace industries, as well as in small engines and electronic packaging applications. In the case of metal matrix nanocomposites, incorporation of as little as one volume percentage of nanosize ceramics has lead to a much greater increase in the strength of aluminum and magnesium base composites than was achieved at much higher loading levels of micron-sized additions. Such potential improvements have great implications for the automotive and aerospace, and, in particular, the defense industries due to the drastic weight savings and exceptional properties that can be achieved. Potential aerospace applications may include ventral fins for aircrafts, as well as fan exit guide vanes for commercial airline jet engines. Both components require high stiffness and strength, low weight as well as resistance to erosion from rain, airborne particulates and hail. Components used in the automotive industry where bulk nanocomposites would likely be valuable include brake system components, which require high wear resistance, and thermal conductivity, intake and exhaust valves, which require high creep resistance and resistance to sliding wear, as well as piston liners, which require high wear resistance, good thermal conductivity and low coefficient of thermal expansion. In addition, exceptionally high thermal conductivities, possible in selected nanocomposites, will find applications in thermal management applications in computers. Metal matrix nanocomposites can be designed to exhibit high thermal conductivity, low density, and matching coefficient of thermal expansion with ceramic substrates and semiconductors, making them ideal candidates for such applications.

Concluding Remarks

There are exciting opportunities for producing exceptionally strong, wear resistant metal matrix nanocomposites with acceptable ductility by solidification processing and powder metallurgy. A fundamental understanding, however, must be gained of the mechanisms that provide these improvements in properties if such materials are to find wider commercial application. Moreover, processing methods must be developed to synthesize these materials in bulk, at lower cost, with little to no voids or defects, and with improved ductility, possibly as a result of bimodal and trimodal microstructures. Metal matrix nanocomposites can lead to significant savings in materials and energy and reduce pollution through the use of ultra-strong materials that exhibit low friction coefficients and greatly reduced wear rates.

References:

(1) Salvetat, J. P.; Andrew, G.; Briggs, D.; Bonard, T. M.; Basca, R. R.; Kulik, A. *J. Phys Rev Lett.* **1999**, *82*, 944. (2) Morgan, A. *Material Matters* **2007**, *Vol. 2 No. 1*, 20. (3) Hassan, S. F.; Gupta, M. *J. Alloys Compds.* **2007**, *429*, 176. (4) Cantor, B. *J. Metastable Nanocryst. Mater.* **1999**, *1*, 143. (5) Guerlotka, S.; Palosz, B. F.; Swiderska-Sroda, A.; Grzanka, E.; Kalisz, G.; Stelmakh, S. *E-MRS* **2003**. (6) Zhou, S.; Zhang, X.; Ding, Z.; Min, C.; Xu, G.; Zhu, W. *Composites: Part A* **2007**, *38*, 301. (7) Rohatgi, P.; Schultz, B.; Gupta, N. *Submitted to Int Mater. Rev.* **2007**. (8) Jun, Q.; Linan, A.; Blau, P. J.; *Proc. of STLE/ASME IJTC* **2006**, 59. (9) Takagi, M.; Ohta, H.; Imura, T.; Kawamura, Y.; Inoue, A. *Scripta Mater*. **2001**, *44*, 2145. (10) El-Eskandarany, M. S. *J. Alloys Compds.* **1998**, *279*, 263. (11) Hong, S. I.; Chung, J. H.; Kim, H. S. *Key Eng Mater.* **2000**, *183–187*, 1207. (12) Islamgaliev, R. K.; Buchgraber, W.; Kolobov, Y. R.; Amirkhanov, N. M.; Sergueeva, A. V.; Ivanov, K. V.; Grabovetskaya, G. P. *Mater. Sci. Eng. A* **2001**, *319–321*, 872. (13) Ferkel H.; Mordike, B. L. *Mater. Sci. Eng. A* **2001**, *298*, 193. (14) Dong, S. R.; Tu, J. P.; Zhang, X. B. *Mater. Sci. Eng. A* **2001**, *313*, 83. (15) Ma, E.; *JOM* **2006**, *58*, 49. (16) Ye, J.; Han, B. Q.; Schoenung, J. M. *Philos. Mag. Lett.* **2006**, *86*, 721.

High-Purity Aluminum

Physical Form	Comments	Purity, %	Prod. No.
Flakes	1 mm, 200 ppm max. trace metals impurities	99.99	**518573-500G**
Pellets	3-8 mesh, 10 ppm max. trace metals impurities	99.999	**326941-25G**
	3-8 mesh, 100 ppm max. trace metals impurities	99.99	**338788-50G**
Rod	3.0 mm × 100 mm	99.999	**202576-10G**
Wire	diam. 1.0 mm, 20 ppm max. trace metals impurities	99.999	**266558-10.5G** **266558-52.5G**
	diam. 0.58 mm, 100 ppm max. trace metals impurities	99.99	**326887-7G** **326887-35G**
Foil	thickness 0.5 mm 20 ppm max. trace metals impurities	99.999	**266574-3.4G** **266574-13.6G**
	thickness 0.25 mm	99.999	**326852-1.7G** **326852-6.8G**
	thickness 0.13 mm	99.99	**326860-900MG** **326860-3.6G**
Powder	<75 µm, 500 ppm max. trace metals impurities	99.95	**202584-10G** **202584-50G**
Nanopowder	<150 nm, 6000 ppm max. trace metals impurities	99.5	**653608-5G**

For more information about these and other related materials, please visit ***sigma-aldrich.com/metals***.

Carbon Nanotubes

Product Name	Outer Diameter (nm)	Inner Diameter (nm)	Length (mm)	Purity (% CNT)	Prod. No.
Single-wall, Carbo-Lex AP-grade	1.2–1.5	NA	2–05	50–70	**519308-250MG** **519308-1G**
Single-wall	1.1	NA	.5–100	>50	**636797-250MG** **636797-1G**
Single-wall, short	1–2	NA	.5–2	>90	**652512-250MG**
Double-wall	5	1.3–2.0	0.5	50–80	**637351-250MG** **637351-1G**
Multi-wall, Arkema CVD	10–15	2–6	.1–10	>90	**677248-5G**
Multi-wall	110–170	–	5–9	>90	**659258-2G** **659258-10G**
Multi-wall, powdered cylinder cores	–	2–15	1–10	10–40	**406074-100MG** **406074-500MG** **406074-1G** **406074-5G**
Multi-wall, as produced	6–20	–	1–5	>7.5	**412988-100MG** **412988-500MG** **412988-2G** **412988-10G**
Graphite, nanofibers	80–200	0.5–10	.5–20	>95	**636398-2G** **636398-10G** **636398-50G**

For more information about these and other related materials, please visit ***sigma-aldrich.com/nano***.

Self-Propagating Reactions Induced by Mechanical Alloying

Prof. Laszlo Takacs
University of Maryland, Baltimore County

Introduction

Mechanical alloying is a "brute force" method of affecting alloying and chemical reactions. The mixture of reactant powders and several balls are placed in the milling jar of a high-energy ball mill, for example, a shaker mill or a planetary mill (**Figure 1**). The collisions and friction between the balls, and between the balls and the wall of the container, result in deformation, fragmentation, mixing, and cold-welding. The reactivity increases due to defect formation and increased interface area, and eventually alloying and/or chemical reactions take place. Neither additional heat nor solvent are needed. The product is a powder that can be consolidated using the usual methods of powder metallurgy. Mechanical alloying is a very flexible technique and has been used to prepare a broad variety of materials, including dispersion-strengthened alloys, amorphous alloys, and nanocomposites.[1] High-energy ball milling is also called mechanochemical processing when used, often in conjunction with other steps, for inorganic synthesis, the processing of minerals, and the activation of building materials.[2]

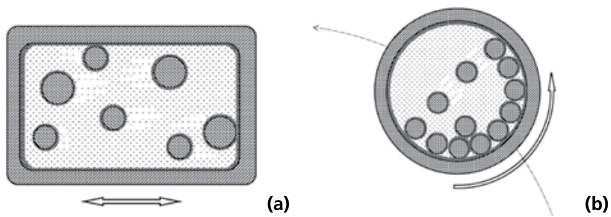

Figure 1. Cross section views of the milling vial of a shaker mill (a) and a planetary mill (b).

Mechanically-induced Self-propagating Reactions (MSR) are possible in highly exothermic powder mixtures.[3] Initially, milling results in activation, similar to any other mechanical alloying process. But at a critical time, called the ignition time, the reaction rate begins to increase. As a result, the temperature rises, further increasing the reaction rate and eventually leading to a self-sustaining process. Most of the reactants are consumed within seconds. At this stage, the reaction is similar to thermally ignited self-propagating high-temperature synthesis (SHS).[4] The abrupt temperature increase is detectable on the outer surface of the milling container and its presence distinguishes such mechanically induced self-propagating reactions (MSR) from gradual processes (**Figure 2**). MSR can happen in a broad variety of systems, such as in Fe_2O_3–Al, Ni–Al, Ti–C, Zn–S, and Mo–Si mixtures.[3] The ignition time is an important attribute of the process; it can vary from a few seconds to several hours depending on the reaction and the milling conditions.

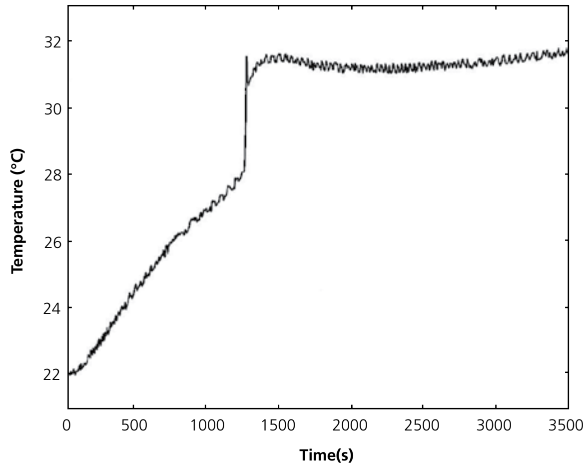

Figure 2. Temperature of the outside surface of the vial during ball milling of a 5 Ni + 2 P mixture in a SPEX 8000 Mixer Mill. Ignition is indicated by the rapid temperature rise at 1220 sec. The gradual temperature increase before ignition is caused by dissipated mechanical energy.

The investigation of MSR contributed considerably to our understanding of mechanochemical processes in general. The variation of the ignition time with process conditions and material properties tells us about the mechanism of the activation process, while detailed studies of partially activated powders provides information about the nature of the critical state. MSR has also been considered as a practical means for the production of useful materials, particularly refractory compounds.[3]

Requirements For Self-Sustaining Reactions

MSR (as well as SHS) require sufficient self-heating to propagate the reaction. A measure of self-heating is the adiabatic temperature, defined as the final temperature, if all the reaction heat is used to heat the products. A rule of thumb is that self-sustaining reactions are possible, if the adiabatic temperature is at least 1800 K. Since the main issue is self-heating at the beginning of the reaction, the quantity $-\Delta H_{298}/C_{298}$ (where H_{298} and C_{298} are reaction enthalpy and specific heat at 298 K), written simply as $\Delta H/C$, is often used as a simpler substitute for adiabatic temperature; $\Delta H/C > 2000$ K is the condition for MSR. This simple condition applies surprisingly well to the most frequently studied classes of reactions, namely combination reactions between a transition metal and a metalloid element (e.g. Ti-B, Nb-C, Mo-Si, Ni-P) and thermite-type reactions between an oxide and a more reactive metal (e.g. Fe_3O_4-Al, CuO-Fe, ZnO-Ti). Much lower values of $\Delta H/C$ are sufficient for MSR with chalcogenides and chlorides. **Table 1** contains data for a few typical reactions.

Mechanical Alloying

Table 1. Typical reactions showing mechanically induced self-propagation and the corresponding reaction heats (ΔH) and ratio of ΔH in the heat capacity of the products (*C*).

Reaction	–ΔH / formula (kJ/mol)	ΔH/C (K)
3 CuO + 2 Al ⇒ 3 Cu + Al_2O_3	1190	7810
4 CuO + 3 Fe ⇒ 4 Cu + Fe_3O_4	461	1850
3 Fe_3O_4 + 4 Al ⇒ 9 Fe + 4 Al_2O_3	3376	6222
5 Ni + 2 P ⇒ Ni_5P_2	436	2867
Sn + 2 S ⇒ SnS_2	154	2189
Ti + 2 B ⇒ TiB_2	316	7111
Hf + C ⇒ HfC	226	6011
Mo + 2 Si ⇒ $MoSi_2$	132	2055

As more exothermic reactions become increasingly easy to self-sustain, reactions with higher adiabatic temperatures are expected to require shorter activation times before ignition. Such a relationship indeed exists, but only if the other material parameters and the milling conditions are very similar. So far, the best correlation was observed for the reduction of CuO (Aldrich Prod. No. **203130**, **450804**, **450812**), NiO (Aldrich Prod. No. **203882**, **637130**, **481793**), Fe_3O_4 (Aldrich Prod. No. **310069**, **518158**, **637106**), Cu_2O (Aldrich Prod. No. **208825**, **566284**), and ZnO (Aldrich Prod. No. **204951**, **255750**, **544906**), with the same metal (Ti, Zr or Hf).[3] These are ductile-brittle systems[5] where milling results in a fine dispersion of the oxide particles in the metal matrix. The development of the microstructure depends primarily on the ductile component and it is kept the same for each series.

The changes caused by mechanical milling during the activation period—decrease of grain size, mixing, and formation of lattice defects—depend mainly on the mechanical properties of the reactants. Although it is difficult to quantify this relationship, the increasing width of the X-ray diffraction lines indicates that the crystallite size decreases and the accumulated lattice strain of the metal component increases as the powder approaches ignition.[6,7] While reducing the grain size and thereby increasing the interface area is certainly a key component of the activation process, agglomeration is also necessary to ensure efficient matter and heat transfer. An interesting case is the reduction of MoS_2 (Aldrich Prod. No. **234842**) with aluminum powder (Aldrich Prod. No. **202584**, **653608**). This reaction is gradual, although $\Delta H/C$ = 2093 K is well over the accepted threshold for an MSR process. However, MoS_2 prevents agglomeration, reducing the area of the active interface.[8]

The mechanical intensity of the milling action depends on the number and energy of the collisions between the milling balls and between the balls and the container wall. The charge is characterized by the ball-to-powder mass ratio, a parameter approximately proportional to the rate of specific energy input. For typical milling conditions, ignition takes place when the powder has received a critical amount of mechanical energy and the ignition time is inversely proportional to the ball-to-powder mass ratio. If too much powder is used, the energy of each individual impact is distributed in a very large volume and the stresses are not large enough to cause activation. If the amount of powder is too little, the heat loss to the milling tools and to the atmosphere quenches any incipient self-sustaining reaction.

Understanding Mechanically Induced Self-Propagating Reactions

A mechanical alloying experiment may look quite simple, but the underlying process is very complex consisting of the components on very different length and time scales. Thus, the complete modeling of a mechanochemical event requires an adequate description of the macroscopic processes, such as the operation of the mill, the collisions between the milling balls, and the transport of the powder within the milling container. On the microscopic scale, the effect of an individual collision on the powder caught between the impacting surfaces must be understood and the formation of lattice defects and the elementary interface reactions must be described. Significant advances were made toward a general theory of gradual mechanical alloying by Prof. Courtney and his students.[9]

The key moment of an MSR is ignition. Once we understand what makes the state of the material critical at ignition, we should be able to use this understanding of MSR for learning about the initial phase of other mechanical alloying processes. Unfortunately, many details are system specific and identifying the general features is consequently difficult. Whether ignition takes place or not may be very sensitive to composition and milling conditions. For example, **Figure 3** shows the X-ray diffraction patterns of two x(Zn+S) + (1–x)(Sn+2S) mixtures.[10] This is an unusual system as the combination reactions

$$\mathrm{Zn} + \mathrm{S} \rightarrow \mathrm{ZnS}$$

$$\mathrm{Sn} + 2\mathrm{S} \rightarrow \mathrm{SnS_2}$$

are both self-sustaining, but the process is gradual in mixtures of the two for $0.19 < x < 0.45$. The pairs of patterns shown in Figure 3 represent two samples just below and above the lower limit. After 33 min of milling, the state of the samples is practically identical. Minutes later MSR takes place in the sample with x = 0.185 and the reaction is practically complete a few seconds later. No ignition is observed in the powder with x = 0.2 and there is little chemical change close to 33 min of milling in this sample. Nevertheless, the powders react gradually and complete transformation is observed after extended milling.

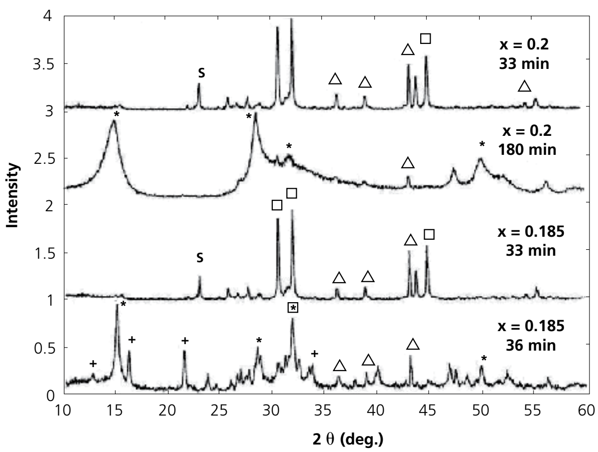

Figure 3. X-ray diffractograms of two x(Zn+S) + (1–x)(Sn+2S) mixtures. The main lines of Sn (□), Zn (Δ), S, SnS (x), SnS_2 (*) and Sn_2S_3 (+) are indicated.

A simple model can be used to describe the degree of activation with an ignition temperature, $T_{ig.}$,[7] i.e. the temperature at which the reaction becomes self-sustaining upon heating. It appears that the ignition temperature decreases with milling, until it becomes lower than the temperature of the hot spots between the colliding balls. At that moment ignition occurs. The advantage of this picture is that the ignition temperature can be determined independently from heating curve measurements. Dramatic reduction of the ignition temperature was indeed found in some systems (e.g. Ti–Si–C but not in others such as Mo–Si)[11,12]. Relaxation and oxidation can be part of the reason; the conditions during uniform heating and ball milling are also very different.

Usually only a fraction of the milled powder is floating around inside the milling vial as free dust. The majority of the material forms a thin coating over the surface of the balls and the walls of the container. The initial hot spots of ignition are created in this coating as small sections of it are compressed energetically between the colliding balls.[9] Whether it expands or extinguishes is a small-scale SHS issue, which depends on the balance between the reaction heat, the local heating, and the heat dissipation into the surrounding powder. A distinguishing feature of MSR is the importance of the heat loss to the milling tools[3] that can delay or prevent ignition if the powder layer is thin (meaning the amount of powder in the container is small).

Examples and Applications

The reduction of a metal oxide with a reactive metal is the most widely studied class of reactions due to the large number of systems with the required high adiabatic temperature. For example, the reduction of CuO with iron is exothermic enough to support an MSR,[7] and reactions between an iron oxide and metals like Al or Ti are also self-sustaining.[3,13] There are many combinations in between. Therefore, it is possible to select groups of reactions where one property varies in a systematic way while the others remain nearly constant. For example, CuO, NiO, Fe_3O_4, Cu_2O, and ZnO (in order of decreasing adiabatic temperature) were reduced with the Group IVB metals Ti (Aldrich Prod. No. **268496**, **366994**), Zr (Aldrich Prod. No. **403288**, **403296**) and Hf (Aldrich Prod. No. **266752**). Surprisingly, the ignition time was the shortest with Zr for each oxide; in the case of Cu_2O the variation is more than an order of magnitude larger (**Figure 4**).[13] This is one of the few examples where the chemical behaviors of Zr and Hf are so different.

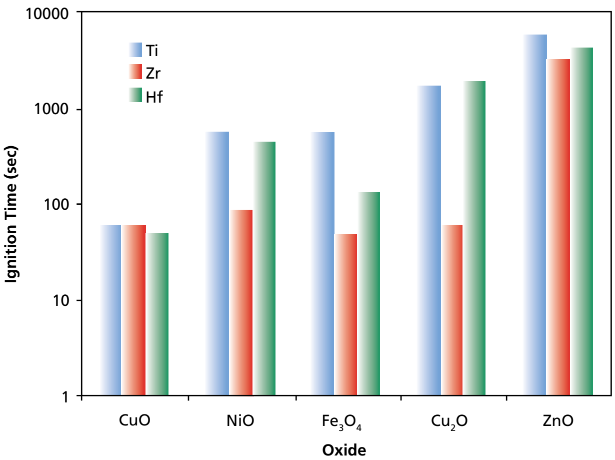

Figure 4. Ignition times of Mechanically Induced Self-propagating Reactions between Cu, Ni, Fe and Zn oxides, and Ti, Zr, and Hf metals.

The formation of NiAl from a mixture of elemental powders is an example of a metal-metal reaction that proceeds as an MSR.[14,15] The experimental conditions need to be selected very carefully, otherwise the reaction progresses gradually. As a rule, however, the formation of other intermetallic compounds is either not exothermic enough, or the efficient heat dissipation to the milling tools prevents ignition in purely metallic systems.

MSR is a promising method for the preparation of refractory metal-metalloid compounds because it is fast, simple, direct, and uses the heat generated by the process itself to reach high temperatures. The main difficulty is that the product is non-uniform and agglomerates immediately after the self-sustaining process. Continued milling can remedy the problem, although it increases the processing time and the possibility of contamination from the milling tools. $MoSi_2$ (Aldrich Prod. No. **243647**) attracted early attention, as it is the primary material of heating elements up to 1700 °C.[6,12] As the reaction between Mo and Si is not very exothermic and two different phases of $MoSi_2$ can form, obtaining uniform product by milling molybdenum and silicon is difficult. The binary carbides, borides and silicides of Ti, Zr, and Hf can be prepared much easier by MSR.[13] Furthermore, Ti_3SiC_2 is a very promising material that combines the high temperature oxidation resistance of ceramics with a level of ductility usually found in metals. The preparation of this compound was successfully carried out by an MSR synthesis using elemental powder mixtures.[16] It is worth noting that due to the possible formation of several phases in the Ti–Si–C system, obtaining the desired single-phase material requires that process parameters be selected and controlled very carefully.

Incorporating nitrogen into an intermetallic compound is always difficult. Ambient nitrogen was used to prepare carbonitrides by milling Nb (Aldrich Prod. No. **262722**, **262749**), Ta (Aldrich Prod. No. **262846, 545007**) or Hf with carbon in a planetary mill.[17] The milling container was permanently connected to the nitrogen supply via a rotary valve and flexible tubing. The composition could be controlled over a wide range by adjusting the carbon content.

MSR and SHS are related processes and both have been utilized for the preparation of refractory compounds. They can also be combined into a process called mechanically activated SHS (MASHS).[18] In MASHS, the mixture of powder components is activated by ball milling, then the powder is pressed into a block and the reaction is ignited thermally in a separate step. Mechanical activation lowers the ignition temperature and results in a more stable combustion process producing a more uniform product than a conventional approach. An interesting example is the formation of $FeSi_2$ from a mixture of iron (Aldrich Prod. No. **255637**, **209309**, **267953**) and silicon (Aldrich Prod. No. **215619**, **267414**, **475238**) powders.

The adiabatic temperature of this reaction is only about 1300 K. Thus, neither conventional SHS nor MSR seem possible. Indeed, neither could be observed. However, utilizing the MASHS process, an appropriate mechanical activation by ball milling increases the reactivity in the system and makes an SHS in a separate step possible.

Conclusion

MSR is an interesting variation of mechanical alloying that contributed substantially to our understanding of the chemical transformations facilitated by ball milling. It also forms a base for potential applications, either alone or in combination with other processing techniques. In particular, it is promising for the preparation of refractory materials.

References:

(1) Suryanarayana, C. *Mechanical Alloying and Milling* (Marcel Dekker, New York, 2004.) (2) Boldyrev, V. V. *Russ. Chem. Rev.* **2006**, *75*, 177.
(3) Takacs, L. *Prog. Mater. Sci.* **2002**, *47*, 355. (4) Merzhanov, A. G. *Combust. Sci. and Tech.* **1994**, *98*, 307. (5) Koch, C. C. *Annu. Rev. Mater. Sci.* **1989**, *19*, 121. (6) Ma, E.; Pagán, J.; Cranford, G.; Atzmon, M. *J. Mater. Res.* **1993**, *8*, 1836. (7) McCormick, P. G. *Mater. Trans., JIM* **1995**, *36*, 161. (8) Takacs, L.; Baláž, P.; Torosyan, A. *J. Mater Sci.* **2006**, *41*, 7033. (9) Courtney, T. H. *Mater. Trans. JIM* **1995**, *36*, 110. (10) Susol, M. A. *Ball Milling Induced Reactions in the Zn-Sn S System* MS Thesis **1995**. (11) Riley, D. P.; Kisi, E. H.; Phelan, D. *J. Eu. Ceram. Soc.* **2006**, *26*, 1051. (12) Takacs, L.; Soika, V.; Baláž, P. *Sol. State Ionics* **2001**, *141–142*, 641. (13) Takacs, L. *J. Sol. State Chem.* **1996**, *125*, 75–84. (14) Atzmon, M. *Phys. Rev. Lett.* **1990**, *64*, 487. (15) Liu, Z. G.; Guo, J. T.; Hu, Z. Q. *Mater. Sci. Eng.* **1995**, *A192–193*, 577. (16) Li, S.-B.; Zhai, H.-X. *J. Am. Ceram. Soc.* **2005**, *88*, 2092. (17) Cordoba, J. M.; Sayagues, M. J.; Alcala, M. D.; Gotor, F. J. *J. Am. Ceram. Soc.* **2007**, *90*, 381. (18) Gras, C.; Zink, N.; Bernard, F.; Gaffet, E. *Mater. Sci. Eng. A* **2007**, *456*, 270.

Binary Metal Alloys

Name	Chem. composition	Comments	Prod. No.
Aluminum-nickel alloy	Al, 50% Ni, 50%	flammable powder	**72240-100G** **72240-500G**
Copper-tin alloy	Cu/Sn, 90/10	Spherical powder, −200 mesh	**520365-1KG**
Iron-nickel alloy	$Fe_{0.55}Ni_{0.45}$	Nanopowder, <100 nm particle size (BET), ≥97%	**677426-5G**
Lithium-aluminum alloy	Li 20% Al 80%	flammable powder	**426490-5G** **426490-25G**
Platinum/iridium alloy (70:30)	Pt/Ir, 70/30	Wire, diam. 0.5 mm	**357383-440MG** **357383-2.2G**
Sodium-lead alloy	Pb/Na, 90/10	Chips, chunks, granules	**359165-25G**
Titanium-copper alloy	Cu, 25% Ti, 75%	Powder, 6–12 µm	**403385-50G**
Zirconium-nickel alloy	Ni, 30% Zr, 70%	Powder, −325 mesh	**403261-100G**
Zirconium-nickel alloy	Ni, 70% Zr, 30%	Powder, −325 mesh	**403253-25G** **403253-100G**

For more information, please visit ***sigma-aldrich.com/matsci***.

Binary Metal Compounds: Carbides, Phosphides, Silicides

Metal	Chem. Composition	Comments	Prod. No.
Carbides			
Aluminum (Al)	C_3Al_4	Powder, –325 mesh, cubic phase	**241873-25G** **241873-100G**
Boron (B)	CB_4	Powder, –200 mesh	**378100-100G** **378100-500G**
		Powder, 10 µm	**378119-50G**
Chromium (Cr)	Cr_3C_2	Powder, –325 mesh	**402680-50G** **402680-250G**
Hafnium (Hf)	HfC	Powder, –325 mesh	**399574-5G** **399574-25G**
		Powder, <1.25 µm	**594636-25G**
Niobium (Nb)	NiC	Powder, 5 µm	**343234-25G**
Molybdenum (Mo)	Mo_2C	Powder, –325 mesh	**399531-50G** **399531-250G**
Silicon (Si)	SiC	Powder, 200–450 mesh	**378097-250G** **378097-1KG**
		Powder, –400 mesh, >90% purity	**357391-250G** **357391-1KG**
		Powder, <100 nm, surface area 70–90 m2/g	**594911-100G** **594911-250G**
Tantalum (Ta)	TaC	Powder, 5 µm	**280801-10G**
Titanium (Ti)	TiC	Powder, –325 mesh	**307807-100G** **307807-500G**
		Powder, <4 µm	**594849-25G** **594849-100G**
		Powder, 130 nm particle size (spherical)	**636967-25G** **636967-100G** **636967-250G**
Tungsten (W)	WC	Powder, 10 µm	**241881-100G**
Zirconium (Zr)	ZrC	Powder, 5 µm	**336351-50G** **336351-250G**
Phosphides			
Calcium (Ca)	Ca_3P_2	99% purity	**400971-100G** **400971-500G**
Gallium (Ga)	GaP	99.99% purity	**521574-2G**
Nickel (Ni)	Ni_2P	Powder, –100 mesh, 98% purity	**372641-10G**
Indium (In)	InP	Pieces, 3–20 mesh, 99.998% purity	**366870-1G**
Iron (P_2Fe)	P_2Fe	Powder, –40 mesh, 99.5% purity	**691593-5G**
Iron (P_3Fe)	P_3Fe	Powder, –40 mesh, 99.5% purity	**691658-5G**
Silicides			
Calcium (Ca)	$CaSi_2$	Technical grade	**21240-250G-F** **21240-1KG-F**
Chromium (Cr)	$CrSi_2$	Powder, –230 mesh, 99% purity	**372692-25G**
Magnesium (Mg)	Mg_2Si	Powder, –20 mesh, 99% purity	**343196-25G**
Niobium (Nb)	$NbSi_2$	Powder, –325 mesh	**399493-10G**
Tungsten (W)	WSi_2	Powder, –325 mesh 99% purity	**399442-10G**
Vanadium (V)	VSi_2	Powder, –325 mesh	**399450-10G**
Zirconium (Zr)	ZrSi2	Powder, –325 mesh 99% purity	**399426-50G**

For more information about these and other related materials, please visit ***sigma-aldrich.com/matsci***.

Ultra Pure Metals
for High Technology Applications

The primary focus of our manufacturing facility in Urbana, Illinois, USA is on the purification of inorganics and metals for a variety of high technology applications. Our capabilities in the area of metals purification utilize several routes to produce some of the purest alkali earth and rare earth metals in the world. These techniques can also be used in the manufacture of alloys and other materials for your research or commercial requirements.

Our proprietary techniques allow us to manufacture barium, calcium, strontium, and magnesium with trace metal purities up to 4N (99.99%). We also manufacture rare earth metals in purities exceeding 4N through a number of different high temperature routes.

One area of customization has focused on the manufacture of prepackaged Molecular Beam Epitaxy (MBE) crucibles for use in thin film manufacturing of advanced materials. We have successfully manufactured high purity barium, calcium, and strontium (as well as other high purity metals) and melted the material into an MBE crucible. This allows for increased loading in the crucible as well as significantly reduced outgassing of the materials in the MBE vacuum chamber. Please contact us today for your specific requirements: **matsci@sial.com**.

High-Purity Metals Manufactured by AAPL—
A Sigma-Aldrich Materials Chemistry Center of Excellence

Metal	Comments	Purity, %	Prod. No
Magnesium (Mg)	dendritic pieces, purified by distillation	99.998 (metals)	**474754-5G** **474754-25G**
		99.99 (metals)	**465992-5G** **465992-25G**
Calcium (Ca)	dendritic pieces, purified by distillation	99.99 (metals)	**441872-5G** **441872-25G**
		99.9 (metals)	**596566-5G** **596566-25G**
Strontium (Sr)	dendritic pieces, purified by distillation	99.99 (metals)	**441899-5G** **441899-25G**
		99.9 (metals)	**460346-5G** **460346-25G**
Barium (Ba)	dendritic pieces, purified by distillation	99.99 (metals)	**474711-5G** **474711-25G**
		99.9 (metals)	**441880-5G** **441880-25G**

Rare earth metal foils are used in thermal and electron beam (e-beam) evaporation processes for coatings and thin films via physical vapor deposition (PVD). The low-temperature e-beam technique is particularly suited for applications such as fuel cells and solar panels. The rare earth metal foils can also be used in the preparation of alloys and composites that contain highly volatile components (Ca, Mg, etc.).

High-Purity Rare Earth Metal Foils

Metal	Dimensions	Purity*	Prod. No.
Lanthanum (La)	25 mm X 25 mm X 1 mm, ~3.9 g	Total REM: 99.5% La/Total REM: 99.9%	**694908**
Cerium (Ce)	25 mm X 25 mm X 1 mm, ~4.2 g	Total REM: 99.5% Ce/Total REM: 99.9%	**693766**
Neodymium (Nd)	25 mm X 25 mm X 1 mm, ~4.4	Total REM: 99.5% Nd/Total REM: 99.9%	**693758**
Samarium (Sm)	25 mm X 25 mm X 1 mm, ~4.9 g	Total REM: 99.9% Sm/Total REM: 99.95%	**693731**
Gadolinium Gd)	25 mm X 25 mm X 1 mm, ~ 4.8 g	Total REM: 99.5% Gd/Total REM: 99.95%	**693723**
Terbium (Tb)	25 mm X 25 mm X 1 mm, ~4.9 g	Total REM: 99.5% Tb/Total REM: 99.9%	**693715**
Dysprosium (Dy)	25 mm X 25 mm X 1 mm, ~5.6 g	Total REM: 99.5% Dy/Total REM: 99.9%	**693707**
Holmium Foil (Ho)	25 mm X 25 mm X 1 mm, ~5.5 g	Total REM: 99.5% Dy/Total REM: 99.9%	**693693**
Erbium (Er)	25 mm X 25 mm X 1 mm, ~5.6 g	Total REM: 99.5% Dy/Total REM: 99.9%	**693685**
Thulium (Tm)	25 mm X 25 mm X 1 mm, ~5.8 g	Total REM: 99.5% Dy/Total REM: 99.95%	**693677**
Ytterbium (Yb)	25 mm X 25 mm X 1 mm, ~4.4 g	Total REM: 99.5% Dy/Total REM: 99.95%	**693669**
Lutetium (Lu)	25 mm X 25 mm X 1 mm, ~6.2 g	Total REM: 99.5% Dy/Total REM: 99.9%	**693650**
Yttrium (Y)	25 mm X 25 mm X 1 mm, ~2.8 g	Total REM: 99.5% Dy/Total REM: 99.9%	**693642**

*REM: Rare earth metals

For more information, please visit *sigma-aldrich.com/metals*.

Argentina
SIGMA-ALDRICH DE ARGENTINA S.A.
Free Tel: 0810 888 7446
Tel: (+54) 11 4556 1472
Fax: (+54) 11 4552 1698

Australia
SIGMA-ALDRICH PTY LTD.
Free Tel: 1800 800 097
Free Fax: 1800 800 096
Tel: (+61) 2 9841 0555
Fax: (+61) 2 9841 0500

Austria
SIGMA-ALDRICH HANDELS GmbH
Tel: (+43) 1 605 81 10
Fax: (+43) 1 605 81 20

Belgium
SIGMA-ALDRICH NV/SA.
Free Tel: 0800 14747
Free Fax: 0800 14745
Tel: (+32) 3 899 13 01
Fax: (+32) 3 899 13 11

Brazil
SIGMA-ALDRICH BRASIL LTDA.
Free Tel: 0800 701 7425
Tel: (+55) 11 3732 3100
Fax: (+55) 11 5522 9895

Canada
SIGMA-ALDRICH CANADA LTD.
Free Tel: 1800 565 1400
Free Fax: 1800 265 3858
Tel: (+1) 905 829 9500
Fax: (+1) 905 829 9292

China
SIGMA-ALDRICH (SHANGHAI) TRADING CO. LTD.
Free Tel: 800 819 3336
Tel: (+86) 21 6141 5566
Fax: (+86) 21 6141 5567

Czech Republic
SIGMA-ALDRICH spol. s r. o.
Tel: (+420) 246 003 200
Fax: (+420) 246 003 291

Denmark
SIGMA-ALDRICH DENMARK A/S
Tel: (+45) 43 56 59 10
Fax: (+45) 43 56 59 05

Finland
SIGMA-ALDRICH FINLAND OY
Tel: (+358) 9 350 9250
Fax: (+358) 9 350 92555

France
SIGMA-ALDRICH CHIMIE S.à.r.l.
Free Tel: 0800 211 408
Free Fax: 0800 031 052
Tel: (+33) 474 82 28 00
Fax: (+33) 474 95 68 08

Germany
SIGMA-ALDRICH CHEMIE GmbH
Free Tel: 0800 51 55 000
Free Fax: 0800 64 90 000
Tel: (+49) 89 6513 0
Fax: (+49) 89 6513 1160

Greece
SIGMA-ALDRICH (O.M.) LTD.
Tel: (+30) 210 994 8010
Fax: (+30) 210 994 3831

Hungary
SIGMA-ALDRICH Kft
Ingyenes zöld telefon: 06 80 355 355
Ingyenes zöld fax: 06 80 344 344
Tel: (+36) 1 235 9055
Fax: (+36) 1 235 9050

India
SIGMA-ALDRICH CHEMICALS PRIVATE LIMITED
Telephone
Bangalore: (+91) 80 6621 9600
New Delhi: (+91) 11 4165 4255
Mumbai: (+91) 22 2570 2364
Hyderabad: (+91) 40 4015 5488
Fax
Bangalore: (+91) 80 6621 9650
New Delhi: (+91) 11 4165 4266
Mumbai: (+91) 22 2579 7589
Hyderabad: (+91) 40 4015 5466

Ireland
SIGMA-ALDRICH IRELAND LTD.
Free Tel: 1800 200 888
Free Fax: 1800 600 222
Tel: (+353) 1 404 1900
Fax: (+353) 1 404 1910

Israel
SIGMA-ALDRICH ISRAEL LTD.
Free Tel: 1 800 70 2222
Tel: (+972) 8 948 4100
Fax: (+972) 8 948 4200

Italy
SIGMA-ALDRICH S.r.l.
Numero Verde: 800 827018
Tel: (+39) 02 3341 7310
Fax: (+39) 02 3801 0737

Japan
SIGMA-ALDRICH JAPAN K.K.
Tel: (+81) 3 5796 7300
Fax: (+81) 3 5796 7315

Korea
SIGMA-ALDRICH KOREA
Free Tel: (+82) 80 023 7111
Free Fax: (+82) 80 023 8111
Tel: (+82) 31 329 9000
Fax: (+82) 31 329 9090

Malaysia
SIGMA-ALDRICH (M) SDN. BHD
Tel: (+60) 3 5635 3321
Fax: (+60) 3 5635 4116

Mexico
SIGMA-ALDRICH QUÍMICA, S.A. de C.V.
Free Tel: 01 800 007 5300
Free Fax: 01 800 712 9920
Tel: 52 722 276 1600
Fax: 52 722 276 1601

The Netherlands
SIGMA-ALDRICH CHEMIE BV
Free Tel: 0800 022 9088
Free Fax: 0800 022 9089
Tel: (+31) 78 620 5411
Fax: (+31) 78 620 5421

New Zealand
SIGMA-ALDRICH NEW ZEALAND LTD.
Free Tel: 0800 936 666
Free Fax: 0800 937 777
Tel: (+61) 2 9841 0555
Fax: (+61) 2 9841 0500

Norway
SIGMA-ALDRICH NORWAY AS
Tel: (+47) 23 17 60 60
Fax: (+47) 23 17 60 50

Poland
SIGMA-ALDRICH Sp. z o.o.
Tel: (+48) 61 829 01 00
Fax: (+48) 61 829 01 20

Portugal
SIGMA-ALDRICH QUÍMICA, S.A.
Free Tel: 800 202 180
Free Fax: 800 202 178
Tel: (+351) 21 924 2555
Fax: (+351) 21 924 2610

Russia
SIGMA-ALDRICH RUS, LLC
Tel: +7 (495) 621 6037
+7 (495) 621 5828
Fax: +7 (495) 621 5923

Singapore
SIGMA-ALDRICH PTE. LTD.
Tel: (+65) 6779 1200
Fax: (+65) 6779 1822

South Africa
SIGMA-ALDRICH SOUTH AFRICA (PTY) LTD.
Free Tel: 0800 1100 75
Free Fax: 0800 1100 79
Tel: (+27) 11 979 1188
Fax: (+27) 11 979 1119

Spain
SIGMA-ALDRICH QUÍMICA, S.A.
Free Tel: 900 101 376
Free Fax: 900 102 028
Tel: (+34) 91 661 99 77
Fax: (+34) 91 661 96 42

Sweden
SIGMA-ALDRICH SWEDEN AB
Tel: (+46) 8 742 4200
Fax: (+46) 8 742 4243

Switzerland
SIGMA-ALDRICH CHEMIE GmbH
Free Tel: 0800 80 00 80
Free Fax: 0800 80 00 81
Tel: (+41) 81 755 2828
Fax: (+41) 81 755 2815

United Kingdom
SIGMA-ALDRICH COMPANY LTD.
Free Tel: 0800 717 181
Free Fax: 0800 378 785
Tel: (+44) 1747 833 000
Fax: (+44) 1747 833 313
SAFC (UK) Free Tel: 01202 712305

United States
SIGMA-ALDRICH
P.O. Box 14508
St. Louis, Missouri 63178
Toll-Free: 800 325 3010
Toll-Free Fax: 800 325 5052
Call Collect: (+1) 314 771 5750
Tel: (+1) 314 771 5765
Fax: (+1) 314 771 5757

Internet
sigma-aldrich.com

Printed on Recycled Paper —
A Worldwide Operation with a Global Commitment

World Headquarters
3050 Spruce St., St. Louis, MO 63103
(314) 771-5765
sigma-aldrich.com

Order/Customer Service (800) 325-3010 • Fax (800) 325-5052
Technical Service (800) 325-5832 • sigma-aldrich.com/techservice
Development/Bulk Manufacturing Inquiries SAFC™ (800) 244-1173

JZX
03394-503403
0107

Accelerating Customers' Success through Leadership in ***Life Science, High Technology*** *and* ***Service***

SIGMA-ALDRICH™

Sigma-Aldrich
3050 Spruce Street
St. Louis, MO 63103 USA
sigma-aldrich.com